Tunable stiffness and crashworthiness of selective laser melted AlSi10Mg sinusoidal auxetic structures

Manpreet Singh, Arun Arjunan, Ahmad Baroutaji, Chameekara T. Wanniarachchi, John Robinson, Abul Arafat, Aaron Vance, Oluwarotimi Lawal, Martin Appiah

PII: S2950-4317(25)00072-3

DOI: https://doi.org/10.1016/j.amf.2025.200262

Reference: AMF 200262

To appear in: Additive Manufacturing Frontiers

Received date: 15 July 2025

Revised date: 17 September 2025 Accepted date: 23 September 2025



Please cite this article as: Manpreet Singh, Arun Arjunan, Ahmad Baroutaji, Chameekara T. Wanniarachchi, John Robinson, Abul Arafat, Aaron Vance, Oluwarotimi Lawal, Martin Appiah. Tunable and crashworthiness of selective laser melted stiffness AlSi10Mg sinusoidal Additive Manufacturing Frontiers (2025), auxetic structures, https://doi.org/10.1016/j.amf.2025.200262

This is a PDF file of an article that has undergone enhancements after acceptance, such as the addition of a cover page and metadata, and formatting for readability, but it is not yet the definitive version of record. This version will undergo additional copyediting, typesetting and review before it is published in its final form, but we are providing this version to give early visibility of the article. Please note that, during the production process, errors may be discovered which could affect the content, and all legal disclaimers that apply to the journal pertain.

© 2025 The Author(s). Published by Elsevier Ltd on behalf of Chinese Mechanical Engineering Society (CMES).

This is an open access article under the CC BY license (http://creativecommons.org/licenses/by/4.0/)

Tunable stiffness and crashworthiness of selective laser melted AlSi10Mg sinusoidal auxetic structures

Manpreet Singh^{a,b,c}, Arun Arjunan^{a,b,c}, Ahmad Baroutaji^b, Chameekara T. Wanniarachchi^{a,b,c}, John Robinson^{a,b,c,d}, Abul Arafat^a, Aaron Vance^a, Oluwarotimi Lawal^{a,b,c}, Martin Appiah^{a,b,c}

^aAdditive Manufacturing of Functional Materials (AMFM) Research Group, University of Wolverhampton, Telford Innovation Campus, Telford TF29NT, United Kingdom

^bSchool of Engineering and Technology, College of Engineering and Physical Sciences, Aston University, Aston Triangle, Birmingham, B47ET, United Kingdom

^aElite Centre for Manufacturing Skills (ECMS), University of Wolverhampton, Springfield Campus, WV10 0JP, UK

^dAdditive Analytics Ltd., Stirchley Road, Telford TF3 1EB, UK

Abstract

This study presents the design, fabrication, and multi-objective optimisation of a novel additively manufactured aluminium sinusoidal ligament auxetic structure (SAS) using AlSi10Mg and Selective Laser Melting (SLM) achieving 99.85% density. Unlike conventional re-entrant designs, the smooth sinusoidal geometry minimises stress concentrations, enhances manufacturability, and provides tunable stiffness and crashworthiness. The SAS lattice, designed with unit cell dimensions of 5×5×3 mm and global dimensions of 30×30×20 mm, demonstrated a negative Poisson's ratio of -0.113 and a compressive elastic modulus of 547 MPa under quasi-static loading (ISO 13314). Finite element analysis (FEA) achieved <3.7% deviation across six key mechanical metrics ranging from E, σ_y , -v, SEA, PCF, and CFE validating numerical predictivity. Response Surface Methodology (RSM) informed by Central Composite Design (CCD) was employed to develop six high-fidelity surrogate models ($R^2 > 0.92$, p < 0.0001), capturing the influence of strut thickness (0.2–0.4 mm) and length (0.5-1.4 mm). Parametric optimisation revealed that strut thickness dominantly controlled stiffness, yield strength, and peak crush force, while strut length significantly influenced Poisson's ratio and crush force efficiency. Three functional optimisation scenarios (S1–S3) yielded tailored structures for stiffness, crashworthiness, and hybrid functionality, achieving maximum SEA of 17.23 kJ/kg and CFE of 73.23%. The results position SAS as a versatile auxetic metamaterial platform with tunable energy absorption for lightweight structural applications.

Keywords: Auxetic metamaterials; Additive manufacturing; Selective laser melting; Energy absorption; Sinusoidal ligament structures.

List of Abbreviations

Abbreviation	Definition
AM	Additive manufacturing
AlSi10Mg	Aluminium-silicon-magnesium
ANOVA	Analysis of variance
BISO	Bilinear isotropic hardening
CAD	Computer-aided design
CCD	Central composite design
CFE	Crush force efficiency
CPU	Central processing unit
EDM	Electrical discharge machining
E	Elastic modulus
FEA	Finite element analysis
LS-DYNA / FE	Finite element (solver)
NPR	Negative Poisson's ratio
PCF	Peak crush force
\mathbb{R}^2	Coefficient of determination
RSM	Response surface methodology
SAS	Sinusoidal Auxetic structure
SEA	Specific energy absorption
SEM	Scanning electron microscopy
SLM	Selective laser melting
UC	Unit cell
$\sigma_{\!\scriptscriptstyle \mathcal{Y}}$	Yield strength
v	Poisson's ratio
t_s	Strut thickness
l_s	Strut length
$ ho_r$	Relative density
S1	Scenario 1
S2	Scenario 2
S3	Scenario 3

1. Introduction

The continual advancements in materials science and manufacturing techniques have given rise to the development of novel structures possessing improved mechanical properties and energy absorption capabilities [1–4]. Auxetic structures, characterised by their ability to exhibit a negative Poisson's ratio, have emerged as a promising class of materials that offer unique attributes [5–9]. The term 'auxetic' to describe materials exhibiting a negative Poisson's ratio was initially introduced by Evans et al. [10]. Unlike traditional materials, auxetics expand transversely when subjected to external forces, enabling

enhanced energy absorption and impact resistance[11–19]. The fabrication of auxetic structures has conventionally been limited by traditional manufacturing processes. However, the advent of additive manufacturing, commonly known as 3D printing, has revolutionised the production of complex geometries and opened exceptional possibilities for tailoring material properties. 3D printing allows for precise control over microstructure, porosity, and architecture, thus providing immense design freedom[20–29]. However, despite the growing body of research on auxetic materials, significant gaps remain in understanding the mechanical behaviour and energy absorption performance of certain auxetic geometries, particularly those based on sinusoidal ligament architectures.

Regarding AlSi10Mg alloy, previous studies have primarily centred on its mechanical properties and microstructural characterisation. Johnson et al. [3] explored the mechanical behaviour of AlSi10Mg alloy under various loading conditions, revealing superior strength and ductility compared to traditional aluminium alloys. In another investigation, Liu et al. [4] studied the microstructure and mechanical properties of 3D-printed AlSi10Mg alloy components, highlighting its potential for lightweight structural applications.

The introduction of additive manufacturing (AM) has revolutionised the fabrication of complex auxetic structures. Selective Laser Melting (SLM), a powder bed fusion technique, allows for the precise control of material properties, geometrical features, and porosity, facilitating the creation of highly customisable metamaterials [30,31]. SLM offers advantages for lightweight metallic auxetic structures, such as those fabricated from AlSi10Mg, an aluminium alloy renowned for its high strength-to-weight ratio, thermal stability, and corrosion resistance [32]. These properties make AlSi10Mg an excellent candidate for applications requiring energy absorption and structural integrity under extreme loading conditions.

A variety of auxetic geometries have been explored in recent literature, including re-entrant, chiral, and rotating rigid structures [18,28,33–55]. Studies on 3D-printed auxetics have demonstrated their superior mechanical properties, with researchers investigating their behaviour under quasi-static, dynamic, and multi-axial loading conditions [56,57]. While previous works have examined polymeric auxetics [58–60], lattice-based metallic auxetic structures [61–66], and functionally graded auxetic materials [67,68], research on sinusoidal ligament auxetic structures (SAS) remains limited. Unlike traditional re-entrant auxetic designs, sinusoidal ligament architectures exhibit a smooth, wave-like deformation that may reduce stress concentrations and improve manufacturability[69]. However, the mechanical response and energy absorption potential of SAS have yet to be thoroughly investigated, particularly when fabricated using SLM-based AlSi10Mg components.

To the best of our knowledge, there is a research gap in exploring the combination of 3D printing technology and AlSi10Mg alloy for fabricating of sinusoidal ligament auxetic structure (SAS). This study addresses this gap by systematically analysing the mechanical behaviour and energy absorption capabilities of 3D-printed AlSi10Mg sinusoidal ligament auxetic structures (SAS). The research focuses on understanding how key geometric parameters, including strut thickness, sturt length, influence key mechanical properties such as elastic modulus(E), yield strength (σ_y), Poisson's ratio (v), and specific energy absorption (SEA), peak crush force (SEA) and Crush Force Efficiency (CFE). Using a combination

of Finite Element Analysis (FEA) and experimental validation, this study provides a comprehensive assessment of SAS architectures, enabling their potential optimisation for lightweight, high-strength, and impact-resistant applications.

2. Materials and Methods

2.1. Design and fabrication

2.1.1. Sinusoidal auxetic architecture

In the case of auxetic materials, the re-entrant structure is one of the most widely utilised design approaches to achieve a negative Poisson's ratio (-v) [70]. Recently, more research has been carried out to develop new auxetic structures from traditional re-entrant structures. For instance, the Sinusoidal ligament can be thought of as a modification of re-entrant structure replacing the sharp chevrons with sinusoidal wave-like architecture. A sinusoidal ligament is an auxetic structure that offers unique mechanical properties. In SAS the auxetic effect is generated by the stretching of the sinusoidal curves. In addition, the sinusoidal ligaments can be changed in response to hinged linear ligaments. Additively manufactured auxetic sinusoidal ligament structures (SAS) are a promising avenue in the field of advanced manufacturing and energy absorption applications. Auxetic structures have high energy absorption and fracture resistance, which makes them suitable for novel applications in defence and the civil sector as body armour, shock-absorbing material, and packaging material.

For cellular materials, the lattice architecture can be defined by the representative volume element which contains the smallest linearly repeatable geometry, called a unit cell (UC) [71,72]. According to Ashby [73], a cellular material is composed of the repeating unit geometry referred to as the unit cells. The relative density and mechanical properties of the unit lattice structure remain unaffected by the number of unit cells (UC) held in its assembly. Informed by the insights from the literature, this work systematically characterises auxetic unit cells (UC) as shown in Fig.1b.

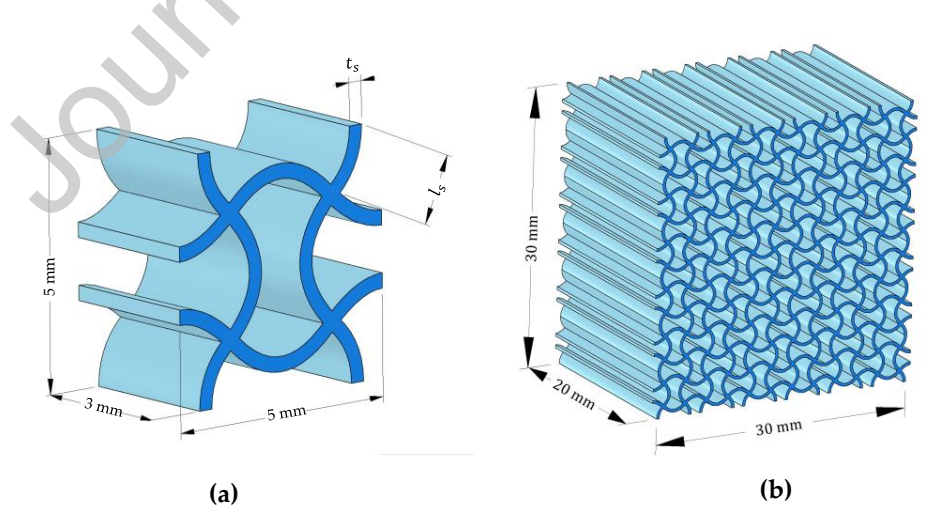


Fig. 1. Three-dimensional schematic of the Sinusoidal ligament structure (SAS) showing (a) the unit cell dimensions along with the variable parameters strut thickness (t_s) and strut length (l_s), and (b) the resulting auxetic lattice architecture with dimensions [74–76].

To minimise the need for extensive support structures during the SLM manufacturing process, the unit cells were designed to ensure that overhangs did not exceed 45°[77–80]. According to Lakes et al. [81] auxetic structures are characterised by their ability to be mechanically adjusted to suit specific requirements. This controllability permits the refinement of properties such as elastic modulus (E) and strength (σ_y) while also allowing unit cell geometries to be adapted for use in various functional and engineering scenarios [82]. To achieve this, the structure must be inherently stable, have a repeating unit cell, and have fewer geometrical parameters. The auxetic cellular structures studied in this research satisfy these criteria. The unit cell geometry was defined with dimensions of 5 mm for both length and height, and 3 mm in width. Upon integration into the lattice framework, each strut was assigned a thickness of 0.3 mm to maintain structural consistency. The sinusoidal ligament -v structure (SAS) was developed by linear mirroring of unit cells in the x and y direction. Informed by the respective unit cells, the auxetic architecture is designated as shown in Fig. 1a. The global dimensions for the lattice structure were 30 mm in x and y and 20 mm along the z direction. The cross-sectional area and length of all the sinusoidal ligament -v architectures (SAS) measured 600 mm² and 30 mm respectively.

2.1.2. 3D printing and powder morphology

The samples were fabricated using the EOS M290 SLM system, which is equipped with a 400 W laser to ensure precise and high-quality manufacturing. AlSi10Mg alloy was selected as the material due to its widespread use in aerospace and automotive applications. This selection is informed by the alloy's low density, high strength-to-weight ratio, notable capacity for energy absorption, strong resistance to impact, and minimal thermal expansion behaviour [83,84]. The AlSi10Mg feedstock, produced via atomisation, is primarily composed of aluminium (Al), silicon (Si), iron (Fe), manganese (Mg), Zinc (Zn) and other trace elements as summarised in Table 1 and the powder morphology as shown in Fig. 2.

Table 1. Chemical composition of AlSi10Mg powder utilised in selective laser melting (SLM) for additive manufacturing [85].

Al	Si	Fe	Cu	Mn	Mg	Ni	Zn	Pb	Sn	Ti
wt%	9.0-11.0	0.55	0.005	0.45	0.25-0.45	0.05	0.10	0.05	0.05	0.15

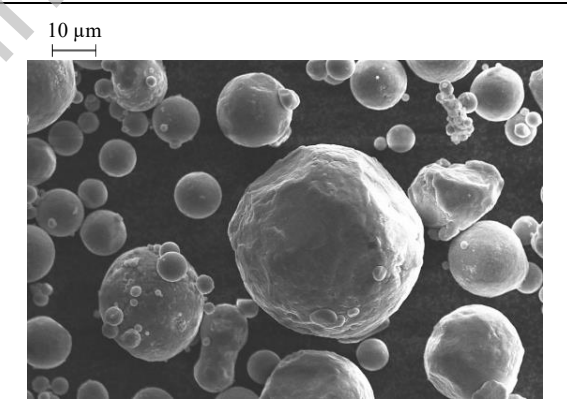


Fig. 2. Scanning electron micrograph of the AlSi10Mg powder feedstock used for selective laser melting.

Due to its composition containing nearly eutectic Al and Si, AlSi10Mg alloy has good weldability [86,87]. This makes AlSi10Mg an excellent choice for the selective laser melting (SLM) additive manufacturing process. The AlSi10Mg metamaterial architecture was fabricated using the selective laser melting (SLM)

additive manufacturing process. The AlSi10Mg feedstock powder was selectively melted using the EOS M 290 SLM system. Auxetic metamaterial specimens were produced on a 250 mm× 250 mm build plate [88–90]. The SLM process parameters namely the laser power, hatch distance, scan speed and layer thickness were specified at 290 W, 0.11 mm, 950 mm/s and 30 µm respectively. In-house prints were carried out to identify the optimum process parameter that will result in 99.85% dense print. This was found to be at 370 W laser power, 1300 mm/s scanning speed, 0.11 mm hatch distance and 30 µm layer thickness. The process took place in a 99.995% Argon environment with oxygen content maintained below ~0.1%. The selective laser melting (SLM) process constructed the sample layer by layer, depositing powder layers each with a thickness of 0.03 mm until the full geometry was formed. The build platform, composed of AlSi10Mg, was preheated to 35 °C prior to the commencement of the printing process [91]. After the initial powder layer is melted, the build platform is incrementally lowered, and a new layer of powder is applied. This process is repeated iteratively until a fully dense part is successfully fabricated.

When printing aluminium alloy, heat treatment is a necessary post-processing step that aids in removing residual stresses brought on by the rapid solidification rates. All the samples were heat-treated at 300°C for 2 hours before removing from the building platform. The heat treatment procedure was informed by previous studies that resulted in good mechanical performance [92,93]. Once thermal post-processing had been completed, the specimens were removed from the build platform using wire electrical discharge machining (EDM). The resulting strut thickness and surface quality were characterised using scanning electron microscopy (SEM). The EVO 50 SEM by Zeiss featuring an incident electron beam that interacts with the sample to generate backscattered and secondary electrons to create an image of the porous scaffold was used [48–52].

2.2. Finite element method

2.2.1. Material behaviour and degree of freedom

The finite element method (FEM) was applied to analyse the non-linear elastic-plastic response of the SAS architectures. The numerical model was developed to closely simulate the structural behaviour observed in experimental tests. To ensure material integrity and prevent self-penetration during the simulation process, the nonlinear explicit mechanical solver in Ansys was utilised. The auxetic lattice structures were digitally designed following established methodologies from previous research. The design models were subsequently imported into the finite element simulations were carried out in ANSYS, with the model geometry imported via the Parasolid format. This approach ensured a high degree of computational precision and consistency throughout the numerical analysis. The Parasolid format was selected for data transfer due to the large geometrical data within the metamaterial architecture to minimise data loss.

Following the evaluation of various element types, the quadratic 20-node SOLID186 element was selected as the most appropriate for this study. This was combined with the bilinear isotropic hardening strain (BISO) model to accurately represent material behaviour. The SOLID186 element was chosen for its ability to capture complex displacement fields with higher precision, outperforming lower-order elements that utilise linear shape functions in displacement estimation. This choice ensured a more

precise representation of the material response during the finite element simulation.[94–96]. The element is described by 20 nodes having three degrees of freedom per node: translation in the nodal x, y, and z directions as shown in Fig. 3(a). The selected element is capable of capturing complex material behaviours, including plastic deformation, nonlinear elasticity, creep, stress-driven stiffening effect, large deflections, and strain effects. Its versatility makes it particularly effective for simulating structures with irregular meshing, ensuring accurate representation of intricate geometries. Additionally, the simulation employs hexahedral elements to enhance computational stability and improve result accuracy [97].

The Bilinear Isotropic Strain Hardening (BISO) material model was selected as the most suitable approach for simulating the auxetic structure, as it effectively captures both elastic and plastic responses[98,99]. This model is characterised by a bilinear stress-strain relationship, where the initial slope is determined by the elastic modulus (E), and the transition to plastic deformation is governed by the yield strength (σ_y). To focus on the overall structural deformation, the post-yield behavior was assumed to follow perfect plasticity.

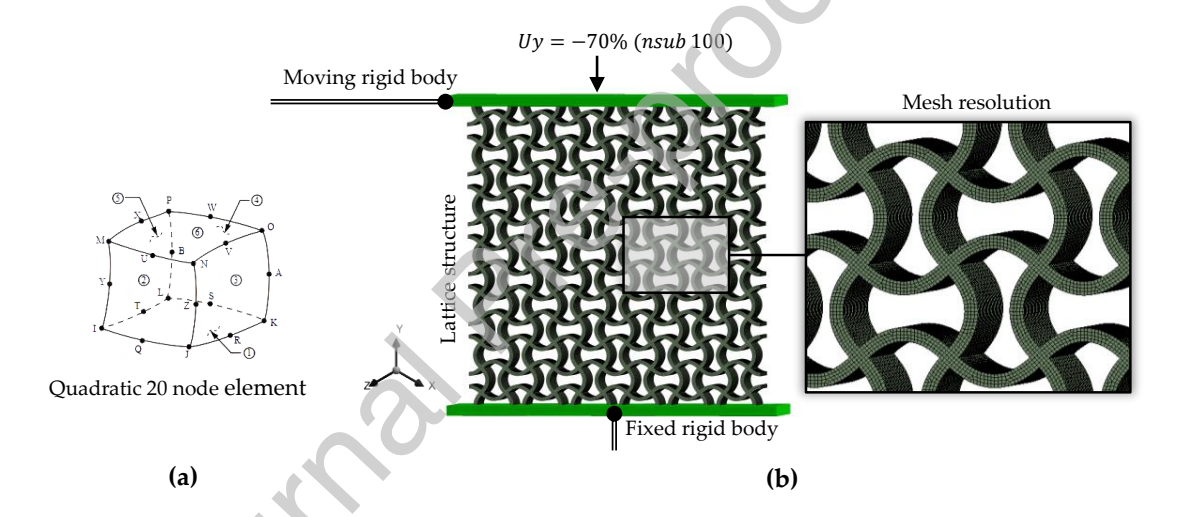


Fig. 3. Finite element model (a) mesh structure using SOLID186 20-node quadratic elements for high geometric fidelity, and (b) boundary conditions applied during compression simulation with fixed lower platen and displacement-controlled upper platen.

To ensure alignment between the numerical model and experimental data, the bulk material properties of AlSi10Mg were derived from tensile test specimens produced using the same process parameters as those employed in fabricating the metamaterial structure. The material properties were calculated. Young's modulus (E) was specified as 68.4 (GPA), yield strength (σ_y) of 268 MPa Poisson's ratio of 0.29 and the bulk density of 2670 kg/m³. While the physical tests of the SAS metamaterial architecture featured prototypes of 30×30×20 mm (length×height×width), the numerical model of SAS architecture was reduced to 30×30×3 mm to reduce the solution time. The influence of reduced thickness on the numerical results was characterised by comparing the two models. The results (Fig. 8) reveal that the reduced model is performing similarly to the full model offering a comparable force-displacement response. This negates the need for a large model and validates that the reduced width model offers comparable results.

The finite element analysis (FEA) results offer a detailed understanding into how the entire structure reacts under applied loads and constraints. In this investigation, two rigid rectangular plates, each measuring 34 mm in length, 6 mm in width, and 0.5 mm in thickness, were positioned on the upper and lower surfaces of the metamaterial architecture, as depicted in Fig. 3b. The auxetic structure remained unconstrained, allowing unrestricted rotation and deformation in all directions, mirroring the conditions of the physical experiment. To minimise numerical artifacts associated with large load increments, the loading process was divided into 100 sub-steps, ensuring high-resolution monitoring of the deformation response.

In the FEA study, the boundary plates were treated as rigid components, with their thickness regarded as negligible owing to their lack of involvement in load transmission within the simulation environment. The bottom plate was fully constrained in all directions, while the top plate was displaced by 70% of the structure's height in the -y direction to mirror the conditions of the mechanical testing within the simulation study, effectively replicating the compressive loading crushing behaviour. A frictional interface with a coefficient of 0.1 was applied between the rigid bodies and the SAS to ensure a realistic representation of contact interactions. To accurately represent the deformation behaviour of the fine beam elements within the structure, large deflection effects were enabled in the simulation. These effects account for both large rotations and large strains, incorporating stress stiffening to enhance the fidelity of the numerical model.

2.2.2. Mesh fidelity

A key factor in developing an accurate finite element model is selecting the optimal mesh discretisation to ensure computational efficiency and solution accuracy. The quality of the mesh plays a critical role in obtaining the best possible solutions from the finite element model. If the mesh is too coarse, the solution will be inaccurate, while a finer mesh will improve the convergence of the numerical model by more accurately capturing stress gradients across an element through the averaging of smaller elements. However, using finer meshes comes at a cost in terms of computing resources due to excessive solution time, which can also lead to generation of substantial amounts of data [100]. As the element density increases, the time it takes to solve the problem also increases, resulting in a need for an effective mesh that balances element density and solution time.

A mesh refinement analysis was performed to evaluate how element size influences the accuracy of the simulation outcomes. This analysis was essential, as changes in mesh density can significantly affect the stress-strain response of the auxetic structure. The study involved carrying out a mesh sensitivity analysis on SAS architecture with a range of element sizes from 0.3 to 0.05 mm as shown in Fig. 4. The model was constraints as shown in Fig. 4. with the SAS structures sandwiched between the top and bottom end plates. The SAS geometry was discretised using 3D 20-node quadratic elements with mesh sizes of 0.30, 0.10, 0.075, 0.06 and, 0.05 mm. Simulations were conducted for each mesh resolution, and the resulting force–displacement curves were analysed to assess variation.

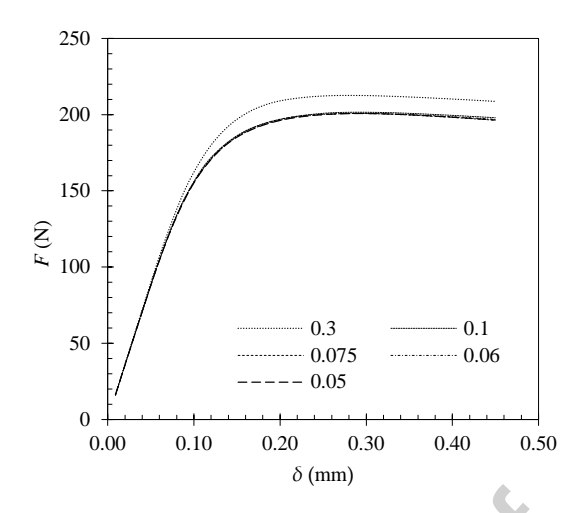


Fig. 4. Mesh convergence study showing force-displacement responses of SAS using varying mesh sizes. Mesh refinement below 0.1 mm yielded stable elastic modulus and yield strength predictions. Final mesh of 0.1 mm ensured numerical accuracy and reduced computation time.

The mesh refinement process was guided by the analysis of force–displacement responses, which served as the principal dataset for evaluating the accuracy of the simulation and the structural performance. The force reaction and axial deformation were analysed to generate force-displacement curves for varying element sizes. As shown in Fig. 4, mesh sizes finer than 0.1 mm showed negligible variation in both the elastic and yield responses of the auxetic structure, thereby confirming numerical convergence. Consequently, element size of 0.1 mm was identified as suitable for reliably capturing the structural stiffness and strength characteristics. The final meshing scheme comprised 773,312 elements and 3,757,303 nodes, requiring a total computation time of 10,396 seconds. The simulations were performed on a computing system equipped with an Intel Xeon 8280 processor running at 2.7 GHz, utilising 56 cores, 1 TB of RAM, and two NVIDIA Quadro GV100 GPUs to improve computational performance.

2.2.3. Poisson's ratio calculation

Poisson's ratio is determined by measuring the material's deformation transverse to the loading direction. It is defined as the ratio of transverse strain to longitudinal strain, as expressed in Eq. 1 [101].

$$v_{yx} = -\left(\frac{\varepsilon_x}{\varepsilon_y}\right). \tag{1}$$

In conventional materials, the Poisson's ratio typically assumes a positive value ($\upsilon > 0$), signifying that axial compression leads to a corresponding lateral expansion. Auxetic materials behave in a fundamentally opposite manner, exhibiting a negative Poisson's ratio. Under axial compression, these materials experience a reduction in their transverse dimensions. In this study, the lateral strain, reflecting horizontal contraction, was derived from finite element simulations by averaging the elastic strain along the principal radial direction, designated as e_x . Strain values were independently assessed across each layer of the Sinusoidal Auxetic Structure (SAS), with the overall transverse contraction represented by

the mean of these values. Subsequently, the negative Poisson's ratio was determined by computing the ratio of the mean lateral strain to the corresponding longitudinal strain (ε_v).

2.3. Prototype testing

Compression testing of the fabricated sinusoidal ligament auxetic structures (SAS) was carried out using a Zwick Roell Z1474 universal test machine (100 kN capacity), configured for high-resolution load–displacement capture (Fig. 5). The machine's servo-driven crosshead operated at a fixed displacement rate of 0.416 mm/s, ensuring quasi-static loading aligned with BS EN ISO 13314 guidelines. Prior to testing, the system was calibrated to BS EN ISO 7500 standards to ensure traceable force accuracy. Three SAS specimens, produced under identical SLM conditions, were tested at room temperature to 70% nominal strain (21 mm displacement). All samples were compressed between flat platens under displacement control until a 50% post-peak load threshold was reached-protecting the system from catastrophic failure. A peak load limit of 80 kN was predefined for safety. To monitor in-situ deformation and capture failure progression, a fixed video tracking system recorded each test. This visual dataset complemented the force–displacement data, which was used to extract stiffness, yield onset, densification behaviour, and specific energy absorption (SEA). Repeat testing confirmed strong reproducibility across all specimens, validating the consistency of the SLM process and the mechanical integrity of the SAS design.

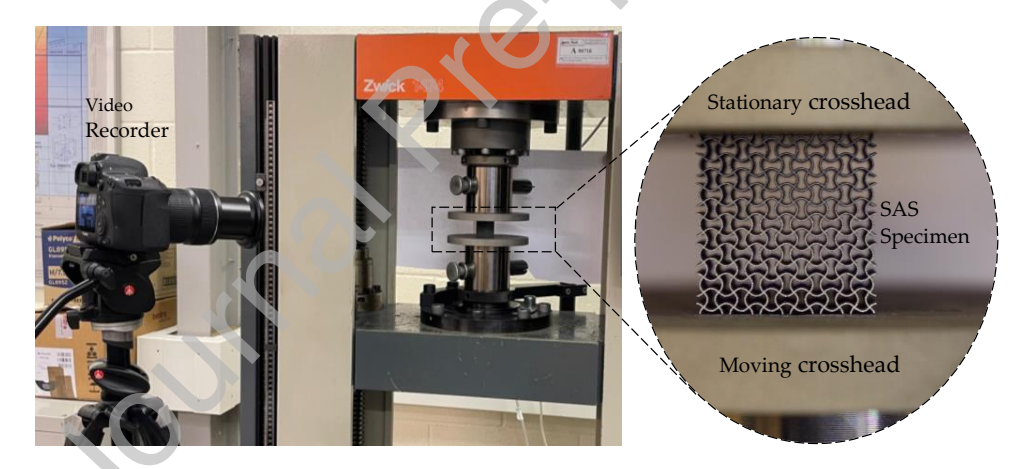


Fig. 5. Experimental compression setup using Zwick Roell Z1474 machine. SAS specimens are compressed quasi-statically at 0.416 mm/s to 70% strain under ISO 13314 conditions. Video capture enables deformation tracking.

2.4. Scanning electron microscopy (SEM)

Scanning Electron Microscopy (SEM) was employed to investigate the morphology of the AlSi10Mg feedstock powder and the surface characteristics of the fabricated SAS samples. SEM is widely used for the characterisation of additively manufactured components because of its ability to resolve sub-micron features at high magnification. Unlike optical microscopy, SEM utilises a focused beam of electrons that interacts with the specimen surface to produce signals such as secondary electrons, backscattered electrons, and characteristic X-rays, which are subsequently detected to form detailed images of the microstructure and surface morphology. In this study, an EVO 50 SEM (Zeiss, Germany) was used,

comprising an electronic console to control key operating parameters (filament current, accelerating voltage, focus, magnification, brightness, and contrast) and an electron column where the beam is generated, focused, and scanned (rastered) across the sample under vacuum using electromagnetic deflection coils. This technique enabled a detailed assessment of particle morphology in the feedstock powder and the surface quality of the printed SAS samples, thereby providing further insight into defect formation and structural integrity [102–104].

In addition to specimen morphology, the role of AM-induced defects was considered when interpreting the mechanical behaviour of the SAS samples. Typical imperfections arising from the SLM process, such as surface roughness, partially fused particles, internal porosity, and dimensional deviations from the CAD geometry, are well documented in the literature [105–108]. These defects reduce the effective load-bearing cross-section of struts and act as local stress concentrators, which can explain the lower stiffness and yield strength observed experimentally when compared with the FEA predictions.

2.5. Surrogate model development

2.5.1. Parametric evaluation

The surrogate model was developed using the Response Surface Methodology (RSM) informed by the Central Composite Design (CCD) algorithm [109,110]. RSM is a mathematical technique that is generally used for design and process optimisation when multiple parameters are at play. Typically, RSM is employed in cases where the input factors exert a significant impact on the quality attribute of the output responses [111,112]. In this context, Response Surface Methodology (RSM) provides a systematic framework for exploring and quantifying the relationships between input variables and their resulting influence on performance indicators or quality-related outcomes. The selection of input variables can be tailored to specific design and optimisation requirements [113].

In terms of structural mechanics, a certain relationship exists between output (y) and design variables (x), where the model can be written as shown in Eq. (2).

$$y = f(x_1, x_2, \dots, x_n) + \varepsilon, \tag{2}$$

where n denotes the number of input variables, and ε represents the random error associated with the response y. In Response Surface Methodology (RSM), when a quadratic polynomial is employed to represent the interaction between the response and the independent variables, the resulting Response Surface (RS) model is formulated as revealed in Eq. (3)

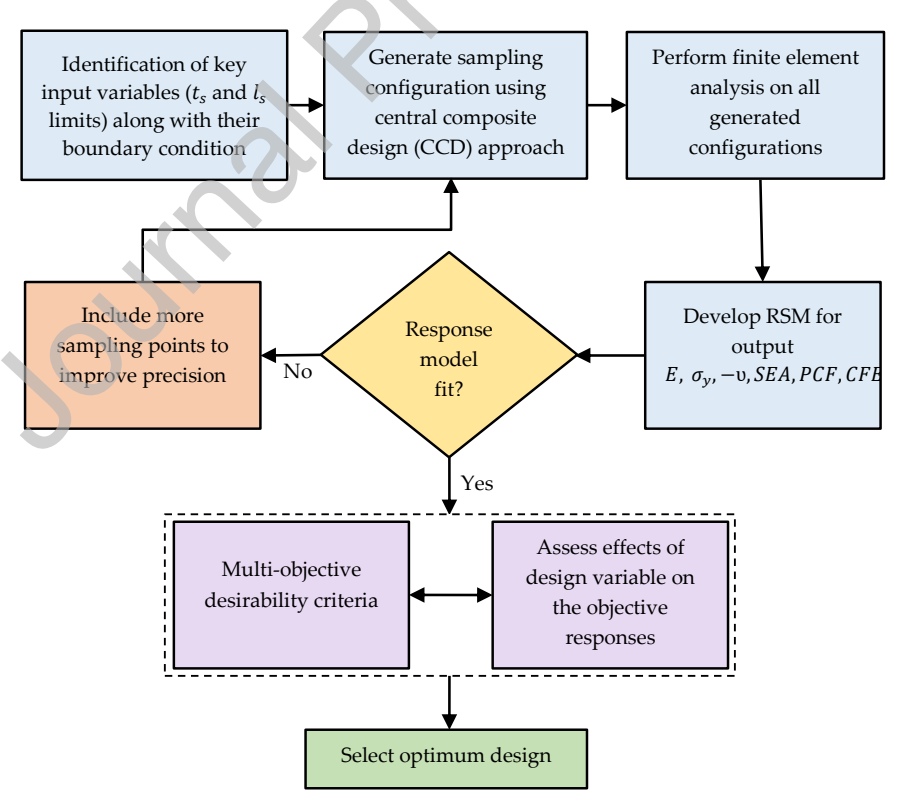
$$y = \beta_0 + \sum_{i=1}^k \beta_i x_i + \sum_{i=1}^k \beta_{ii} x_i^2 + \sum_i \sum_j \beta_{ij} x_i x_j + \varepsilon.$$
 (3)

Regression coefficients (β_0 , β_i , β_{ij} and β_{ii}) serve as statistical estimators that quantify the influence of predictor variables on the corresponding responses. After analysing the randomised experimental data and calculating the beta parameters, the response surface model can then be applied to determine the input values x that correspond to a desired set of output responses. These models are particularly

effective for conducting parametric studies, enabling the evaluation of individual variable effects on the target responses (-v, σ_v , E, SEA, PCF, CFE).

The variation of porosity with respect to and t_s and l_s was also examined. Increasing t_s reduces porosity by raising the relative density of the lattice, while increasing l_s increases porosity through the extension of the ligament length relative to the unit cell dimensions. These dependencies highlight the strong coupling between geometry and porosity and confirm that porosity is implicitly governed by the chosen design variables. The parametric linking of the variables t_s and l_s to the performance -v, σ_y , E, SEA, PCF and CFE. The response surface model is employed for characterisation, allowing both the individual and combined effects of design variables on the target response to be examined and predicted. This approach allows the surrogate model to determine the relative significance of each design parameter, ranking them from highest to lowest impact on the structural performance.

The surrogate models are developed by fitting the results of the training matrix to suitable polynomial equations informed by randomised experimental sets. Developing a surrogate model in this regard is advantageous as it can be used to predict the performance of a given design for a large range of design alternations using limited sets of experiments referred to as sampling points. The study utilises the overall methodology summarised in Fig. 6 to develop the surrogate model and validate its accuracy for optimisation. The training algorithm is guided by the central composite design (CCD), a higher-order sampling method that facilitates the development of accurate response surface models using a reduced number of experimental runs.



 $\textbf{Fig. 6.} \ \ \text{Methodology for the generation of surrogate model for the SAS meta-lattice system.}$

In the context of the current investigation, the design parameters of the SAS need to be linked with the corresponding responses to obtain a solution for the optimisation problem. The description of the optimisation problem is proposed in three different scenarios (Scenario 1-3). The surrogate model is then used to investigate the influence of geometrical parameters and their interactions on the relevant desired responses.

Table 2. Design variable selected for the SAS to be optimised for scenario 1-3.

		Variables		
l _s ,	Limits -	t_s (mm)	l_s (mm)	
	min.	0.20	0.50	
	med.	0.30	0.95	
t_s	max.	0.40	1.40	

Identifying and controlling the contribution of the design requires extracting their geometrical parameters. Here two primary variables are identified as shown in Table 2 namely: the strut thickness (t_s) and strut length (l_s) . The variation of these geometric parameters on the elastic, plastic, and overall performance of the auxetic architecture is characterised.

Table 2 summarises how these variables correspond to the auxetic architecture that is acting as the foundation for optimisation based on Scenarios 1 to 3. The strut thickness (t_s) ranges from 0.2 to 0.4 mm as it offers a reasonable balance between the quality expected from the selective laser melting process and the ability of the structure to deform adequately under loading. The strut length (l_s) was varied from 0.5 to 1.4 mm as this range was found not to induce global buckling informed by the height of the structure. The strut length (l_s) will also alter the angles between all connecting struts so the maximum feasible strut length is 1.4 mm without penetrating the adjacent struts. When it comes to the strut length, reducing it lower than 0.5 mm leads to non-auxetic behaviour due to inadequate porosity. Although there is a slight variation between the ideal and additively manufactured (AM) samples in terms of t_s and l_s , its influence on the -v was found to be only 2.8%, as presented in Table 5 for the SAS. At no stage did this minor variation in the AM samples result in a positive Poisson's ratio. Therefore, a 2.8% deviation is insufficient to alter the strain direction of the architecture.

2.5.2. Optimisation

A multi-objective optimisation Framework is a useful approach for finding solutions that satisfy multiple objectives simultaneously [114]. In the context of this study, the optimisation problem is formulated using the response surface model developed and presented in the previous section. Multi-objective optimisation is a crucial aspect of multiple-criteria decision-making, enabling the identification of optimal solutions that meet the desired objectives. This approach involves simultaneously optimising multiple conflicting objectives, ensuring that the final solution satisfies the criteria for objective desirability [115]. The criteria for desirability can encompass a diverse range of objectives that are closely tied to the design variables and parametric responses. Arjunan et al. [116] demonstrated the application of multi-objective optimisation using the response surface model for auxetic materials. Their research

highlighted the significant benefits of employing multi-objective optimisation to identify solutions that effectively meet multiple objectives.

In summary, multi-objective optimisation represents a suitable and effective methodology for addressing problems involving multiple objective functions, as demonstrated in this study. Eq. 4 presents the standard preparation of the optimisation problem, demonstrating the correlation between the objective function and the associated variables.

$$\begin{cases}
\min. f(s) = [f_1(s), f_2(s), \dots, f_l(s)], \\
s.t. \qquad s^l \le s \le s^u,
\end{cases}$$
(4)

where $s = (s_1, s_2, ..., s_k)$ is the vector of k design variables, s^l and s^u are the lower and upper limits of the design variables, respectively, and f(s) is the objective function [117]. The parametric analysis also revealed the wide potential of this architecture to offer targeted functionality by controlling the design parameters. Consequently, Table 3 demonstrates the multi-objective optimisation of the SAS architecture for three scenarios namely S1, S2 and S3.

Table 3. Summary optimisation scenarios and their objectives to optimise the SAS.

Optimisation scenario	S1	S2	S3
Elasticity modulus (<i>E</i>)	Maximise (1)	None	Maximise (1)
Poisson's ratio $(-v)$	None	None	None
Yield strength (σ_y)	Maximise (↑)	None	Maximise (1)
specific energy absorption (SEA)	None	Maximise (↑)	Maximise (†)
Crush force efficiency (CFE)	None	Maximise (↑)	Maximise (†)
Peak crush force (PCF)	None	Minimise (↓)	Minimise (↓)

While the parametric analysis of the auxetic structures revealed the influence of design variables on key responses namely: -v, σ_y , E, SEA, PCF, CFE the optimal combination of variables that generate the most favourable outcomes has not yet been determined. In order to optimise the SAS, it is necessary to identify the specific design parameters that produce the desired response characteristics. These target responses represent the performance criteria considered most advantageous for the intended application of the design.

Three optimisation scenarios (S1-S3) were examined to determine the most suitable structural parameters for the SAS, as summarised in Table 3. To fulfil the objectives of S1, the optimum architecture must incorporate design parameters that promote high E and σ_y . This scenario can be suitable in optimising auxetic architecture for lightweight applications where high stiffness and strength are required. S2 targets improving the crashworthiness performance signified by high SEA and CFE while maintaining the low PCF. This scenario reflects a situation in which auxetic architectures are specifically designed to maximise crashworthiness performance. S3 provides a balance of elastic and plastic behaviour, targeting applications that demand high stiffness, strength, and energy absorption. It represents a case in which

auxetic structures are engineered to deliver both lightweight performance and enhanced crashworthiness.

3. Results and Discussion

3.1. Specimen morphology and failure mode analysis

Three SAS specimens (*n*=3) were fabricated without the need of support structures, due to the submillimetre scale of the unit cell features and the presence of only short overhangs, as illustrated in Fig. 7(a). The SAS samples were fabricated with the build direction oriented along the z-axis while the stairstep effect can influence inclined features, the surface roughness observed in this study is more strongly attributed to partially fused particles, balling phenomena, and the layer-wise scanning strategy inherent to the SLM process. These mechanisms, together with geometric effects, contributed to the irregular surface finish and are considered as key factors influencing the discrepancy between experimental and numerical results. A comparison between the average porosity of the additively manufactured SAS specimens and the corresponding CAD model values is presented in Table 4. The SLM-produced samples exhibited porosity values ranging from 80% to 88%, which is lower than the ideal porosity range of 88% to 93% observed in the original CAD geometry.

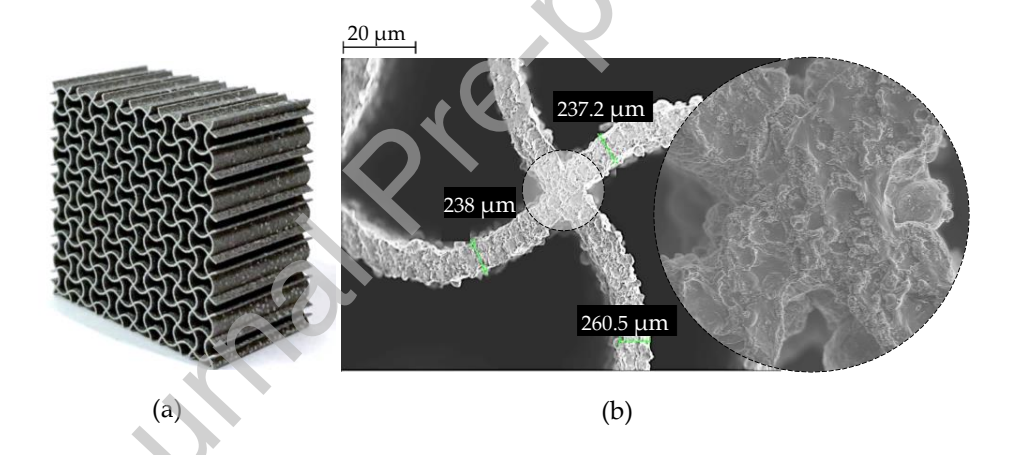


Fig. 7. SEM characterisation of SLM-fabricated SAS showing (a) overall printed lattice, and (b) close-up of struts showing partially melted powder and surface roughness due to stair-step effect.

SEM was utilised to examine both the porosity and structural integrity of the additively manufactured SAS architecture in greater detail. As presented in Fig. 8b, SEM imaging of the sample following shot blasting reveals that the process effectively removed the majority of loosely bound and partially melted powder particles. However, upon closer examination of the joint regions also shown in Fig. 7b residual semi-molten particles were still detectable. Although these features exist at the micron scale, their cumulative presence at several joints may contribute to the overall reduction in porosity, consistent with the findings reported by Arjunan et al [118].

Table 4 Comparison of meta-material porosity between fabricated prototypes and CAD.

Properties		Lattice prototyp	pes
rroperties	CAD	SLM	% Difference

Porosity (%)	90.15	80.87	9.276
1 010010 (, 0)	, 0.10	00.02	, . <u></u> , o

The printed meta-materials exhibited a noticeably rough surface finish, primarily attributed to the stair-step effect inherent to the SLM process. While the overall geometry and interconnected porosity of the fabricated structures closely resembled those of the original CAD models, the average strut thickness showed a deviation of approximately 40–60 μ m. Such deviations are well-documented in the existing literature on SLM-fabricated thin struts with dimensions below 300 μ m [119–121]. This variation in strut thickness contributed to a cumulative decrease in total porosity of around 9.276% relative to the idealised design, as detailed in Table 4.

When comparing the strut thickness variations observed in this study to those documented in prior work, Benedetti et al. [122] mentioned that struts aligned with the build direction are often oversized. This is primarily attributed to the laser spot size exceeding the intended strut diameter. Furthermore, the accumulation of partially fused particles on strut surfaces can exacerbate these dimensional inconsistencies. As illustrated in the SEM image in Fig. 7(b), the findings of this study are consistent with those in the literature, revealing deviations from the nominal 300 µm design without causing a significant change in overall porosity. Notably, the observed difference in strut thickness was mainly influenced by the alignment of the struts, with vertical struts tending to be undersized, whereas horizontal ones appeared oversized [123].

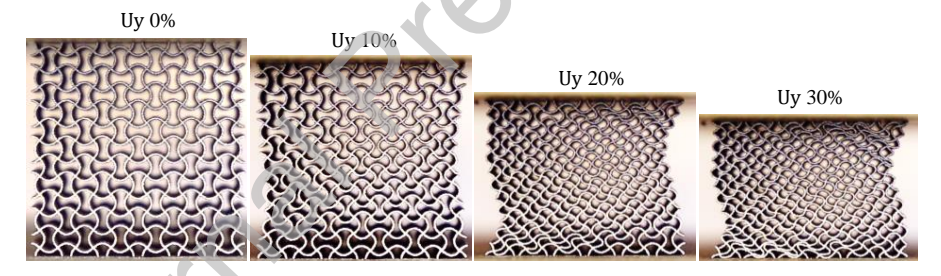


Fig. 8. Deformation of the SAS structure showing 0%, 10%, 20% and 30% deformation under quasi-static compression.

The deformation sequence of the SAS structure under quasi-static compression is presented in Fig. 8. At 0% strain, the lattice maintains its as-printed geometry with well-defined sinusoidal ligaments. At 10% strain, the architecture exhibits a pronounced inward lateral contraction, confirming the auxetic effect during the elastic regime. By 20% strain, localised plastic deformation initiates in the form of crush bands at the upper and lower regions, while the central portion retains structural integrity. At 30% strain, the uniform folding of the sinusoidal ligaments becomes evident, with progressive rotation and bending of the wave-like struts producing a half-wave ligament shape. This collective ligament flexure shortens the distance between nodes in both in-plane directions, driving a sustained negative Poisson's ratio and high crush force efficiency. These observations confirm that the auxetic deformation mechanism of the SAS is dominated by ligament flexure and rotation, which govern its energy absorption capacity.

3.2. Numerical evaluation

3.2.1. Finite element model validation

The FEA model effectively replicates the elastic and plastic behaviour of SAS metamaterials. Table 5 presents the precision of the numerical FEA model in predicting key mechanical properties, including the E, σ_y , SEA, PCF, and CFE of the SAS structure studied. When compared to experimental test data obtained under similar conditions, the numerical findings exhibit similar trends across all cases considered. Notably, the elastic modulus predicted by the model deviates from the physical test data by only 0.18%, while the yield strength shows a difference of 3.08%.

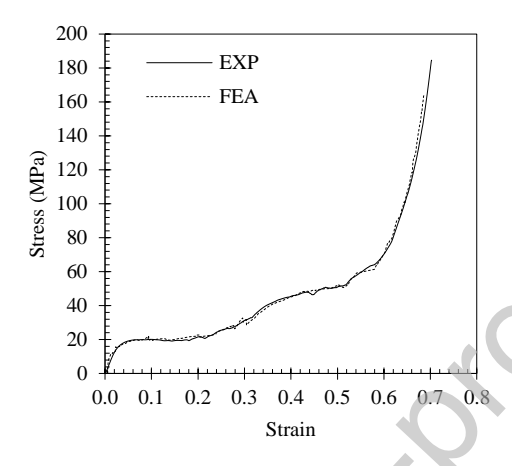


Fig. 9. Comparison of stress-strain curves from FEA simulation and physical compression tests.

Regarding Poisson's ratio, which characterises the relationship between lateral and axial strains in the Sinusoidal Ligament Auxetic Structure (SAS), a difference of 2.80% was observed. The difference in SEA and PCF was 3.22% and 2.62% respectively. Although the FEA model developed has been validated to predict the trend in mechanical performance with sensible accuracy, as shown in Table. 5, differences in the predicted of CFE values of up to 3.64% were observed which is considered satisfactory [109].

Table 5. Comparison between the FEA and the experimental data.

Properties	FEA	EXP	% Difference	
E (MPa)	548	547	0.18	
σ_y (MPa)	9.75	10.05	3.08	
υ	-0.111	-0.114	2.66	
SEA (kJ/kg)	6.22	6.02	3.22	
PCF (N)	5820	5972	2.62	
CFE (%)	54	52	3.77	

The observed differences between the FEA and experimental results are largely attributable to the inherent characteristics of the SLM process. Previous studies [124,125] have extensively documented that SLM induces geometric deviations arising from the stair-step effect and the presence of partially fused powder on component surfaces. These manufacturing artefacts become progressively significant in porous and geometrically intricate thin-walled structures, such as those examined in the present study. While the experimental data inherently reflect all structural imperfections, the FEA model of the SAS is based on an idealised CAD geometry, assuming a homogeneous and defect-free structure. Furthermore, the rough surface finish an intrinsic characteristic of SLM-fabricated SAS samples-can substantially affect

the mechanical behaviour, especially when beam and wall thicknesses are comparable. Nevertheless, the comparison between the FEA and experimental test data reveals a strong correlation, thereby validating the model's accuracy and confirming its suitability for further predictive analyses.

The largest deviation between numerical and experimental results was observed for the crush force efficiency (CFE), with the FEA predicting 54% compared to the SLM experimental value of 52%, corresponding to a relative error of 3.77%. This discrepancy arises primarily from the assumptions embedded in the finite element model. First, the geometry in FEA is idealised, meaning cell walls are perfectly smooth, defect-free and dimensionally uniform. In comparison, the additively manufactured specimens inevitably incorporate stair-stepping, partially melted particles, and sub-surface porosity. These imperfections locally reduce stiffness and promote earlier buckling or damage initiation, lowering the experimental average crush force relative to the model. Second, the constitutive law employed in the FEA represents the post-yield plateau as a simplified hardening response without explicit damage accumulation or densification behaviour. In practice, the SLM microstructure exhibits localised softening, microcracking, and gradual densification, which diminish the sustained load-bearing capacity and hence the average force. Together, the geometric idealisation leading to a slight over-prediction of peak crush force, and the lack of damage/softening leading to an over-prediction of the plateau translate into a modest but systematic overestimation of CFE. However, the relative error remaining below 4% is well within the range typically regarded as acceptable for lightweight structure design and optimisation. Moreover, this level of fidelity provides confidence that the model is sufficiently robust for parametric studies and surrogate design, while also highlighting clear directions for refinement, such as incorporating stochastic defect fields from micro-CT data and adopting a crushable-foam model with progressive damage to capture the true post-yield response of SLM materials.

3.2.2. Stress distribution

Stress concentration within the SAS is largely dictated by the geometry of its unit cells and their connectivity. Regions experiencing elevated stress may initiate early plastic deformation, potentially compromising the overall strength, stability, and long-term durability of the SAS. The FEA results indicate that stress distribution follows a predictable pattern, with the highest concentrations occurring at specific joint regions where struts intersect. According to Salimon et al.[126], a relationship between the σ_y and the ρ_r of auxetic cellular structures was established, although certain inconsistencies were observed between experimental results, potentially due to stress concentration. Previous studies [360–362] have shown that certain design configurations are particularly vulnerable to stress concentrations, which can trigger the premature initiation of plastic failure in the SAS.

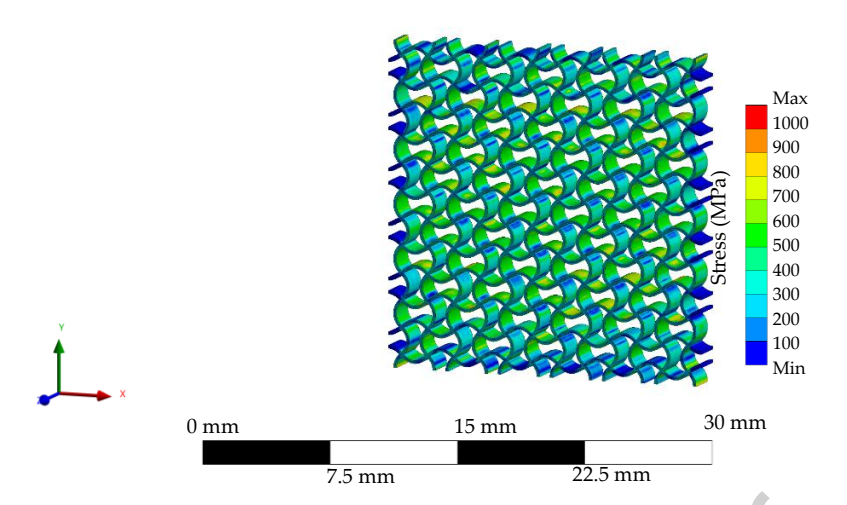


Fig. 10. FEA-derived stress distribution in the SAS lattice under compressive loading. High stress concentration is minimised at curved junctions, contributing to improved strength and reduced failure initiation in comparison to re-entrant designs.

Finite element (FE) modelling generates extensive datasets, and its close agreement with experimental results allows for detailed structural analysis. As shown in Fig. 10, the stress distribution across the SAS architecture highlights regions of localised stress. The SAS demonstrates superior stiffness and strength, attributed to reduced stress concentration. A consistent colour legend supports the visual comparison of stress intensity across different configurations, while Fig. 9 also reports the corresponding values of σ_{max} relative to the material's yield strength.

SAS exhibits the lowest stress concentration, characterised by a more uniform stress distribution. The observed development in stress concentration correlates alongside the reduction in yield strength, suggesting that the decrease in strength is primarily attributed to stress concentration effects. Under elastic compression, the macroscopic stress developed within the SAS structure is directly proportional to the applied ε . As the structure performance primarily depends on the UC shape rather than the ρ_r . FEA results indicate that stress concentration is influenced by the geometry of the unit cell and its connectivity with neighbouring UCs. Thus, designs with the highest stress concentration exhibit lower values of σ_y . The SAS architecture demonstrates superior stiffness and strength, which can be attributed to its reduced stress concentration relative to other commonly used auxetic designs.

3.3. Surrogate precision

The impact of design variables was examined across six key response metrics, including -v, σ_y , E, SEA, PCF, and CFE. The results of this study demonstrate that the surrogate models developed using RSM and CCD are effective in predicting the responses of SAS under different design variable variations. The models provide insights into the relationship between the design variables and the desired responses, allowing for the identification of optimal design parameters for SAS. The findings of this research have practical implications for the design and development of the SAS for various applications, including impact protection, energy absorption, and structural reinforcement.

The analysis further includes an assessment of the approximation model's quality, which effectively captures the behaviour of -v, σ_y , E, SEA, PCF, and CFE for the SAS. The Analysis of Variance (ANOVA) is used to assess the accuracy of the surrogate model in capturing the desired responses. Additionally, the influence of the control variables, namely strut thickness (t_s) and strut length (l_s), on the mechanical performance and energy absorption behaviour of the SAS. The optimisation description is conceived as three different scenarios which target the mechanical performance, energy absorption characteristics and then a combination.

Table 6 Central Composite Design (CCD) matrix of design variables and corresponding responses used to train the SAS approximation model.

Fac	tors	Responses					
A	В	1	2	3	4	5	6
t_s	l_s	-v	σ_{y}	E	SEA	PCF	CFE
(mm)	(mm)	-	(MPa)	(MPa)	(kJ/kg)	N	%
0.30	0.50	-0.104	4.200	580	8.867	1070.500	63.993
0.20	0.95	-0.115	1.900	150	9.185	648.530	75.783
0.30	0.95	-0.113	3.900	500	12.898	1547.500	66.599
0.37	0.63	-0.104	5.100	1010	15.608	2553.800	58.254
0.30	0.95	-0.113	3.900	500	12.898	1547.500	66.599
0.40	0.95	-0.109	7.800	1169	18.060	3171.800	60.508
0.30	0.95	-0.113	3.900	500	12.898	1547.500	66.599
0.30	0.95	-0.113	3.900	500	12.898	1547.500	66.599
0.23	1.27	-0.120	2.250	215	7.5970	0960.750	71.401
0.30	1.40	-0.123	4.000	418	14.551	1777.800	66.735
0.23	0.63	-0.109	2.000	252	10.984	0983.340	67.940
0.30	0.95	-0.113	3.900	500	12.898	1547.500	66.599
0.37	1.27	-0.120	6.000	812	18.771	2793.400	70.264

The central composite design (CCD) approach was employed to develop the training matrix and perform a parametric investigation based on the design variables t_s and l_s for the SAS structure. Prior to performing the parametric analysis, the accuracy of the surrogate models was assessed using the ANOVA methodology. Following the successful validation, the surrogate models were employed to generate response surface models, evaluating the relationship amongst geometrical parameters t_s and l_s and several performance responses, including -v, σ_y , E, SEA, PCF, and CFE

A higher-order CCD approach was utilised to construct the surrogate model, identifying the key independent variables listed in Table 6. To satisfy the sampling needs for the training dataset, multiple SAS design configurations were created, each reflecting the designated factorial parameter combinations. Subsequently, the finite element method was used to model and analyse each of the design samples, to obtain their respective response for -v, σ_y , E, SEA, PCF and CFE to complete the training model as presented in Table 6. Informed by the numerical analysis, the outcomes of the training matrix were computed to reveal surrogate models as shown in Eq. (5)-(1)0, targeting all the six responses of interest. The effects of t_s and t_s on σ_y , PCF, and t_s are described by linear expressions, represented by Eq. (5)-

(7), respectively. Conversely, *E*, SEA, and CFE display a nonlinear, quadratic relationship with these geometric parameters, as indicated in Eq. (8)-(10).

$$\sigma_{v} = -4.324 + 26.859t_{s} + 0.340l_{s},\tag{5}$$

$$PCF = -2482.476 + 12324.080t_{s} + 478.194l_{s}, \tag{6}$$

$$v = -0.1 + 0.023t_s - 0.021l_s, (7)$$

$$E = 0.064 - 2.711t_s + 0.396l_s - 1.788t_s l_s + 15.588t_s^2 - 0.022l_s^2,$$
(8)

$$SEA = 20.771 - 79.702t_s - 10.302l_s + 72.784t_sl_s + 101.124t_s^2 - 4.454l_s^2,$$
(9)

$$CFE = 113.467 - 246.615t_s - 10.291l_s + 94.990t_s l_s + 165.092t_s^2 - 5.581l_s^2.$$
(10)

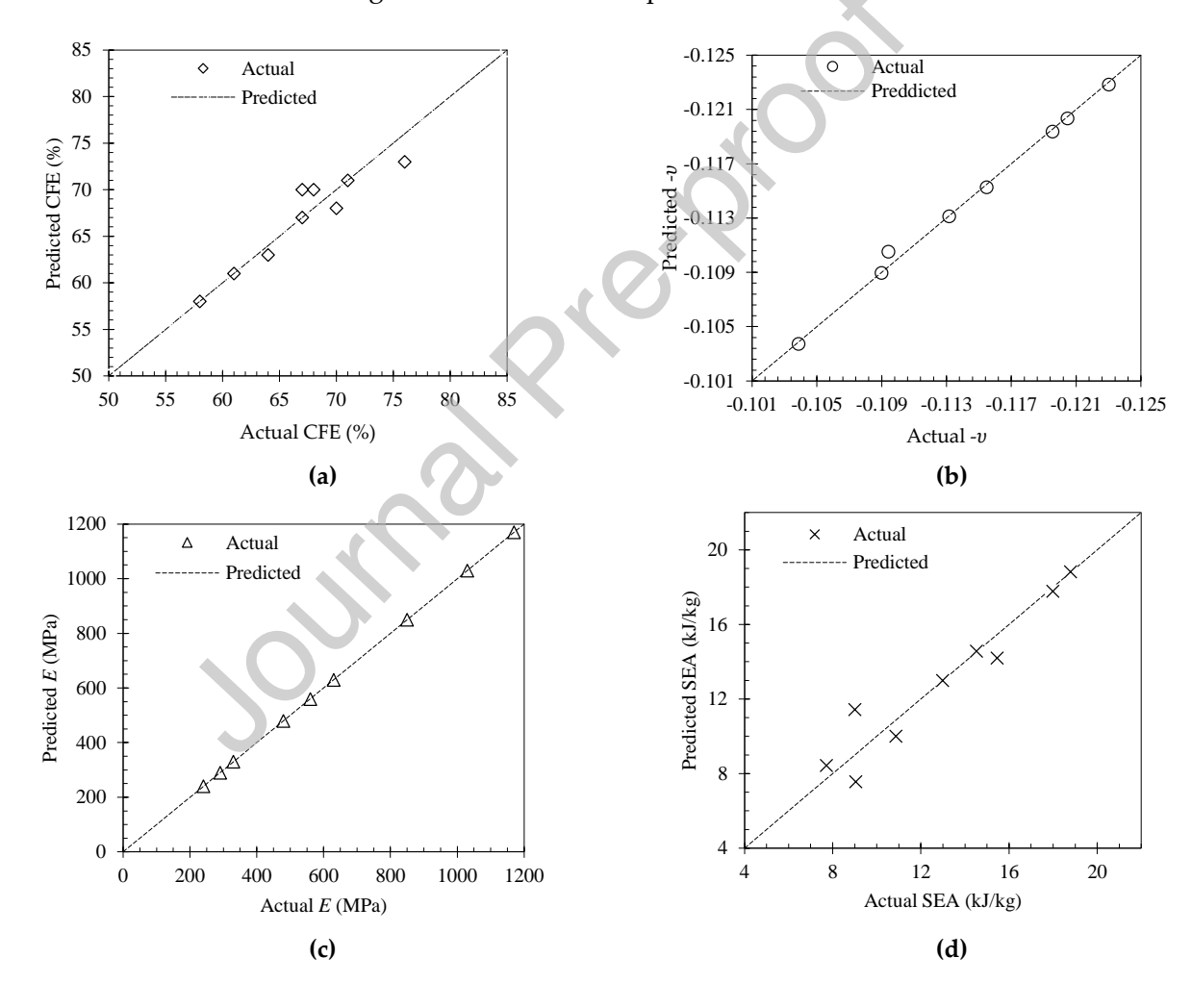
Although a surrogate model has been successfully generated, ANOVA needs to be carried out to characterise the accuracy of each of the models before they can be employed for parametric analysis. The accuracy measures include the probability (p-value), coefficient of determination R^2 , Adjusted R^2 , Predicted R^2 , and Adequate precision. ANOVA shows that the mechanical performance of SAS is significantly influenced by its geometrical parameters. The adequacy measures of the surrogate model demonstrate high accuracy, indicating accurate predictions can be made for all the six response parameters considered. This implies that the approximation models outlined in Eq. (5)-(10) are capable of exploring the design space and reliably predicting mechanical and energy absorption performance.

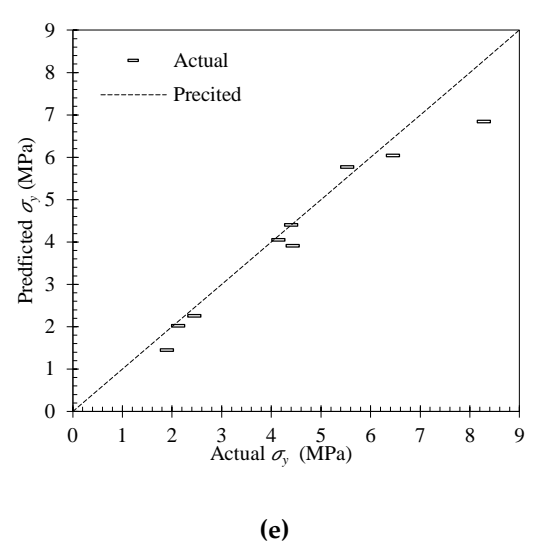
Table 7. Analysis of variance (ANOVA) results for the response surface model applied to the SAS structure.

Model	T 1		Statistical me	easurements			
	<i>F</i> -value	<i>p</i> -value	R^2	$Adj - R^2$	Adeq – precision		
σ_y	065.25	<0.0001	0.928	0.914	23.741		
υ	243.64	< 0.0001	0.979	0.975	44.588		
E	188.38	< 0.0001	0.992	0.997	43.406		
SEA	028.61	< 0.0001	0.905	0.873	17.117		
PCF	062.36	< 0.0001	0.925	0.910	22.901		
CFE	017.42	< 0.0004	0.853	0.804	13.369		

Table 7 demonstrates the each of six models attribute high F-value (>17.42) along with exceptionally low p-value (<0.0004), confirming that all six surrogate models are statically substantial featuring very low noise levels. Typically, model terms with p-value less than 0.001 are considered significant [127]. Additionally, models with sufficient accuracy ratio exceeding four indicate minimal noise within the mode [116]. Furthermore, all models achieved high R^2 values (greater than 0.85), indicating strong alignment with their respective adjusted R^2 values. The analysis of variance confirms that all six SAS models are statistically robust and well-suited for further parametric studies and for analysing variable interdependencies.

Among the six surrogate models, the CFE model exhibited the lowest statistical strength, with R^2 =0.853 and Adeq-precision of 13.369 as shown in Table 7. Although the model is highly significant (p<0.0001), its correlation is weaker than those of the other responses. This reduced strength arises from the inherent variability of CFE, which is a ratio that combines sensitivities from both the peak load and the post-yield plateau, making it inherently more sensitive to small experimental fluctuations, localised imperfections in SLM parts, and numerical scatter in the design matrix. In additively manufactured structures, such sensitivities are further compounded by local defects, surface roughness, and residual stresses from SLM, which cannot be fully captured in simplified surrogate representations. As a result, a greater proportion of variance (~15%) remains unexplained compared to the other models. Nonetheless, the Adeq-precision remains comfortably above the threshold of 4, indicating that the signal-to-noise ratio is sufficient for design navigation. Consistent with ranges reported for reliable predictive models [128,129] this provides confidence that the CFE surrogate retains value for optimisation.





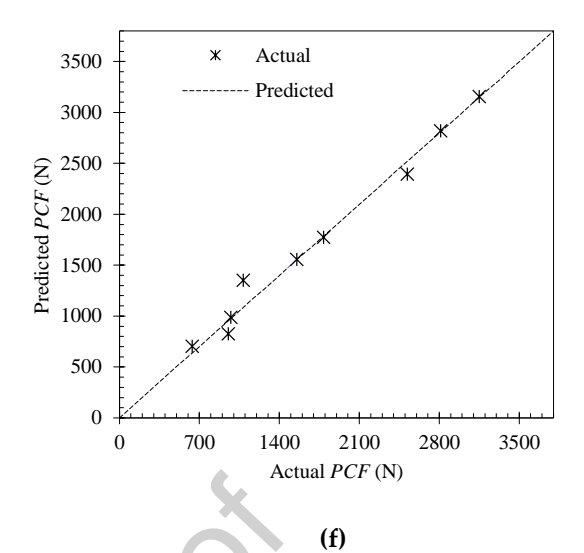


Fig. 11. Validation of surrogate models against FEM results for six mechanical responses showing (a) crush force efficiency, (b) Poisson's ratio, (c) elastic modulus, (d) specific energy absorption, (e) yield strength, and (f) peak crush force; Dotted lines represent ideal prediction, demonstrating high correlation ($R^2 > 0.92$).

Following the assessment of the response surface model's accuracy through ANOVA, its predictions were compared with the numerical simulation results, as illustrated in Fig. 11. This comparison was carried out for all six response variables: CFE (Fig. 11(a)), Poisson's ratio -v (Fig. 11(b)), elastic modulus E (Fig. 11(c)), specific energy absorption SEA (Fig. 11(d)), yield strength σ_y (Fig. 11), and PCF (Fig. 11(f)). To avoid confusion, the predictions of the surrogate are represented using a diagonal dotted line which is used as the reference and the finite element predictions are presented using different markers Overall, the numerical predictions exhibit a strong alignment with the surrogate model predictions. The relatively small residuals, as shown in Table 7, additionally validate the accuracy of the models. These results demonstrate that Eq. (5)-(10) successfully capture the influence of geometric parameters on the associated performance measures. This validates the reliability of the approximation models in predicting all six responses and modelling parametric interactions within the SAS structure.

Table 8. Percentage residuals of the surrogate models showing deviation from an ideal.

CFE (%)	<i>−v</i> (%)	E (%)	SEA (%)	σ_y (%)	PCF (%)
3.03	0.38	0.50	1.73	7.14	3.81
2.38	0.26	4.19	3.05	2.89	3.68
0.00	0.09	0.00	0.00	4.10	7.85
0.00	0.19	2.98	1.08	1.71	6.48
0.00	0.09	0.00	0.00	4.10	7.85
3.32	1.47	3.77	4.76	1.59	8.52
0.00	0.09	0.00	0.00	4.10	7.85
0.00	0.09	0.00	0.00	4.10	7.85
0.29	1.00	1.91	1.13	0.89	1.14
3.22	0.32	0.76	8.04	5.25	5.99
3.96	0.64	1.37	8.29	2.50	3.36

0.00	0.09	0.00	0.00	4.10	7.85	
4.13	1.34	4.26	1.81	1.17	3.61	

3.4. Parametric influence on macroscopic responses

3.4.1. Crush force efficiency

The results shown in Fig. 12 highlights CFE was significantly impacted by both t_s and l_s . A slightly quadratic correlation can be seen in Fig 12(a), with CFE decreasing consistently with t_s . This is due to an increase in peak crush force facilitated by the increasing t_s of the SAS. As the t_s increases, the cross-section of the load-bearing beams increases, leading to higher stiffness and higher σ_y . As a result, the onset of plastic failure informed by the PCF increases drastically, this in turn decreases the CFE, as shown in Fig. 12(a). Although not as significant impact in comparison to t_s , the t_s was similarly found to substantially affect CFE, as shown in Fig. 12(b). This occurs because of the influence of strut length on the curvature at the joints of the unit cell. Larger loads cannot be transferred to the lateral connections at higher t_s due to the increased rotation lowering the PCF.

When crashworthiness is prioritised, the CFE model should therefore be interpreted with caution. Its lower R^2 means predictions are less deterministic than for SEA or PCF, but the model still captures meaningful trends and can guide the identification of promising regions in the design space. In practice, optimisation outcomes involving CFE should be corroborated by targeted validation runs. Thus, in Scenario S2, CFE is best considered in combination with SEA and PCF both of which are described by stronger surrogate fits so that crashworthiness optimisation balances robustness with predictive reliability.

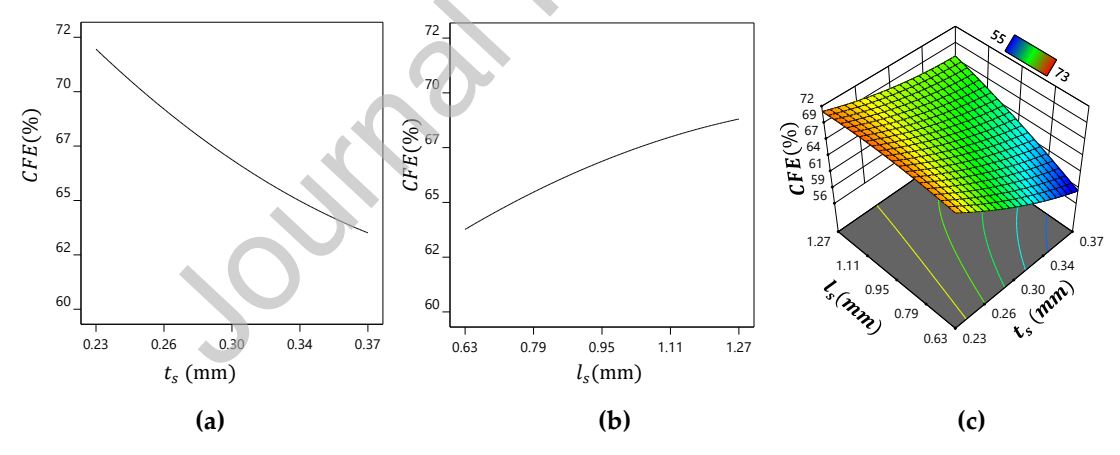


Fig. 12. Effect of strut parameters (a) strut thickness shows inverse quadratic relationship due to increased PCF, (b) strut length shows nonlinear influence via joint flexibility, and (c) combined interaction of t and θ on CFE performance.

The reduced angle at the joints also increases stress concentration which also informs the early onset of plastic failure. This means that the PCF decrease as the l_s increases leading to an increase in CFE. As observed, both design variables independently influence the exhibiting opposite trends, as illustrated in Fig.12(c). As a result, CFE was found to be increased by decreasing the t_s and decreasing l_s . As a result, the highest value of CFE was observed at the maximum l_s and lowest t_s . It was found that t_s is

predominantly affected on CFE, closely followed by l_s . Overall, the first-order effect of t_s is the most significant, followed by l_s and finally, the interaction effect of $t_s l_s$.

3.4.2. Negative Poisson's ratio

The -v is influenced by both t_s and l_s as shown in Fig. 13. However, t_s seems to have a relatively smaller influence in comparison to l_s as shown in Fig. 13a. nevertheless, a linear relationship can be seen for both cases with a value of -v decreasing consistently at t_s increases. This can be attributed to the fact that the ρ_r of the material significantly affects its deformation behaviour. An increase in t_s leads to a higher ρ_r , which enhances the structural strength by providing more material to resist plastic deformation effectively. Overall, while both the l_s and t_s influences the resulting -v they oppose each other in trend as shown in Fig. 13(a) and 13(b).

While both t_s and l_s influence the -v of the sinusoidal ligament auxetic structure (SAS), the effect of l_s is notably more significant. This is primarily due to its role in load transmission within the unit cell. At greater values of l_s , a larger portion of the load is transferred to the lateral connections, which increases lateral deformation and enhances the -v. Consequently, reducing l_s beyond a certain threshold can cause a transition in Poisson's ratio from negative to positive. The analysis indicates that -v increases with higher l_s and lower t_s , with the maximum -v observed at the combination of the largest l_s and the smallest t_s . Among the parameters studied, l_s has the greatest impact on -v, followed by t_s . The linear influence of t_s proves to be the most dominant, followed by the individual effect of t_s , and finally, the interaction effect of t_s , in the order $t_s > t_s > t_s > t_s t_s$.

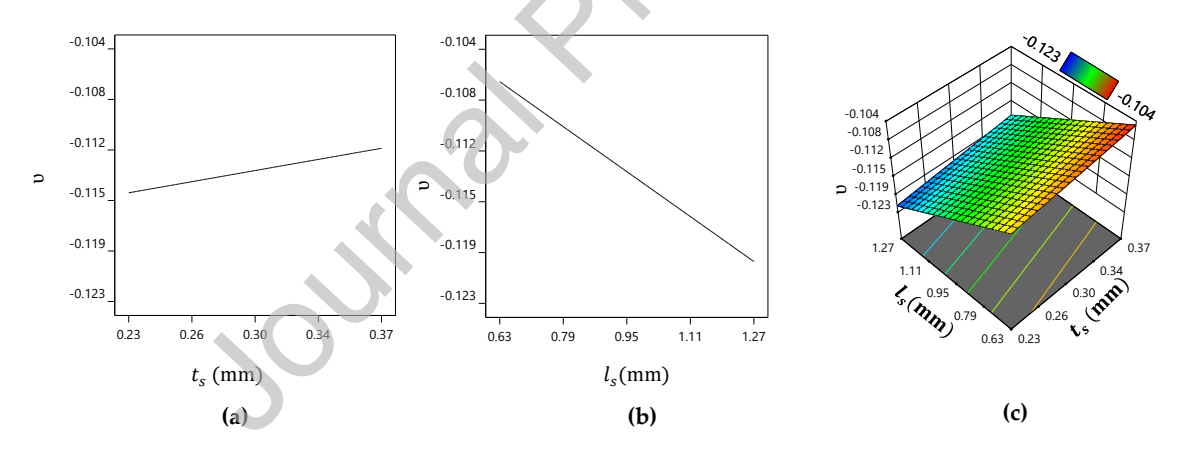


Fig. 13. Variation of Poisson's ratio (a) strut thickness, (b) strut length, and (c) interaction with auxetic angle.

3.4.3. Elastic modulus

A parametric analysis of the elastic modulus of the Sinusoidal ligament auxetic structure (SAS) was carried out and the results revealed that the modulus was largely influenced by the strut thickness (t_s) with a small contribution from strut length (l_s) as shown in Fig 14(a) and 14(b), respectively. This can be attributed to the fact that the porosity of the material significantly affects its deformation behaviour. An increase in thickness leads to a higher relative density, which strengthens the structure by offering greater material resistance to plastic deformation.

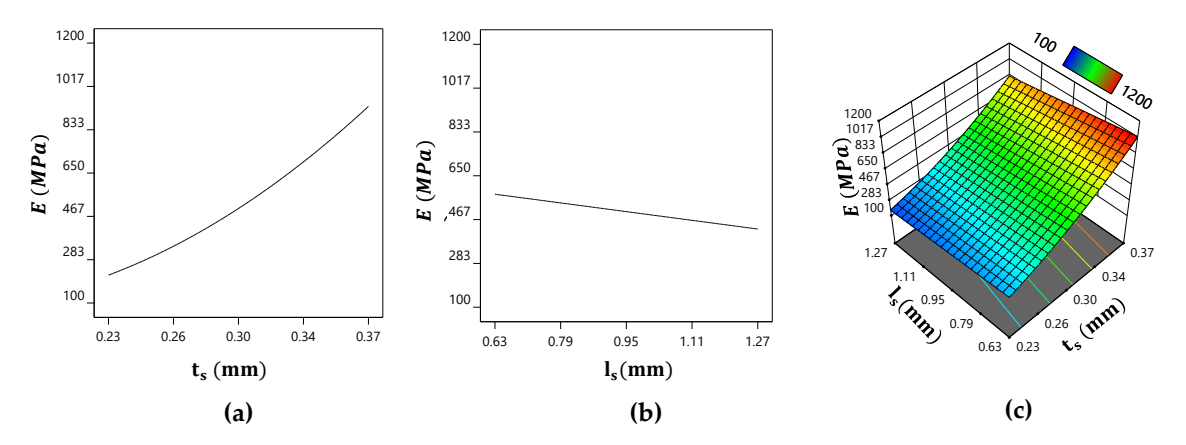


Fig. 14. Dependence of elastic modulus on design parameters: (a) Thickness shows linear increase in stiffness; (b) Length has minimal influence; (c) Interaction effects indicating local reinforcement through increased strut overlap.

While a quadratic relationship was witnessed to represent that relationship between t_s and E, l_s showed a linear trend that is opposite to t_s . This means that increasing t_s consistently increase the elastic modulus. On the contrary, increasing l_s reduces the elastic modulus at a comparatively smaller rate. This cumulative opposing trend on the overall performance of E is signified by Fig. 14(c) revealing a trend in performance that indicates a low-level interaction between the design parameters and the elastic modulus. The highest elastic modulus was observed when both t_s and l_s were at their highest values. Overall, the order of influence of the design variables on the elastic modulus of SAS was found to be $t_s > l_s > t_s l_s > t_s^2 > l_s^2$. Previous literature has shown that auxetic architecture acquires several advantages over conventional counterparts [130] including stiffness control which is confirmed by the observations here.

3.4.4. Specific energy absorption

In comparison to previous responses, SEA was found to be largely influenced by the strut thickness with a minor effect from strut length as shown in Fig. 15. A slightly quadratic relationship can be observed in both cases explaining the relationship between t_s (Fig. 15(a)) and l_s (Fig.15(b)) with the resulting specific energy absorption (SEA).

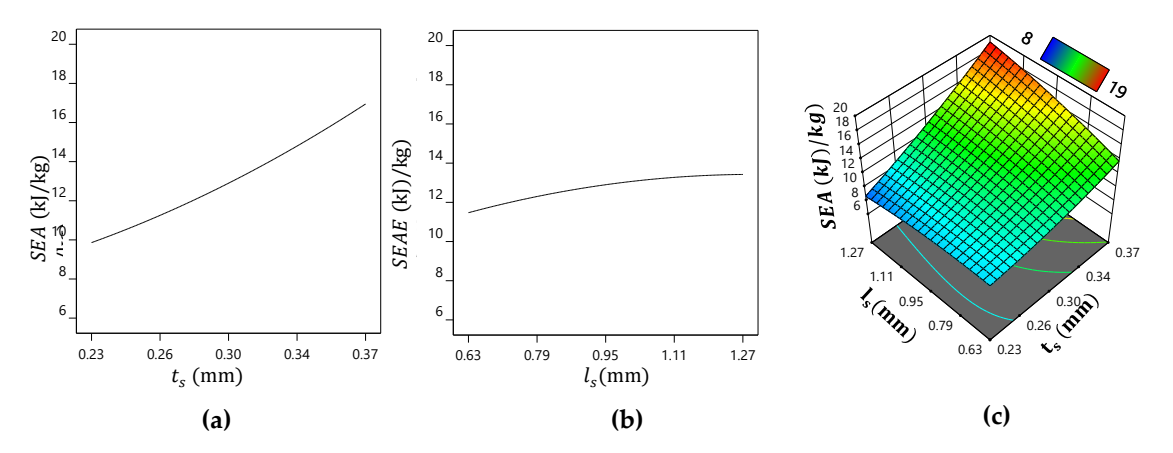


Fig. 15. Impact of design parameters on SEA: (a) Strut thickness strongly improves energy absorption; (b) Strut length provides moderate tuning; (c) Combined increase of both yields maximum SEA of 17.23 kJ/kg.

As shown in Fig. 15(a), SEA can be seen to increase consistently with an increase in t_s in a quadratic fashion. This is due to the influence of the total energy absorbed architecture on influencing the SEA calculation: since SEA is calculated as the ratio of the total energy absorbed and mass, a lower thickness offers lower energy absorbed and vice versa. Correlating this with the trend observed in Fig. 15(a), it is clear that the increase in strut thickness increases SEA.

Although not as significant in comparison to strut thickness, the strut length was also found to influence SEA due to the influence of strut length on the curvature at the joints of the unit cell, as shown in Fig. 15(b). At higher l_s the relative density decreases reducing the mass of the architecture which results in increased SEA. Overall, the interaction effects indicate that highest value of SEA occurs when both l_s and t_s are at the maximum values. Consequently, t_s has the most significant impact on SEA, followed by l_s . Overall, the order of influence can be expressed as $t_s^2 > t_s > t_s l_s > l_s$ with the most significant parameter being thickness and the interaction effects of strut thickness and length.

3.4.5. Yield strength

Fig. 16(a) reveals that the strut thickness has a major influence on the strength of the SAS structure with a linear relationship. Conversely, Fig. 16(b) shows that the effect of strut length (l_s) on the yield strength is negligible, as indicated by an almost straight line across the tested range.

Therefore, t_s is identified as the most significant parameter for modulating the yield strength of the SAS auxetic architecture. Furthermore, the independence of the design parameters on σ_y was analysed, as presented in Fig. 16(c). The results demonstrate that the effect of the design variables on σ_y is minimum and has no significant impact on the performance pattern, resulting in a steady performance slope regardless of l_s variants. Consequently, increasing t_s is the only viable option to enhance the yield strength of the SAS auxetic architecture.

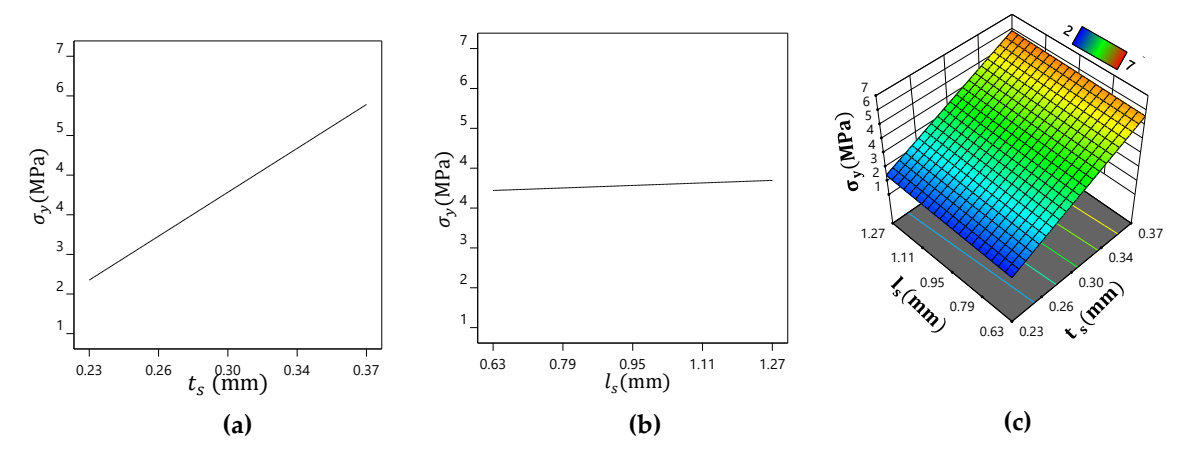


Fig. 16. Effects on yield strength revealing (a) linear increase with strut thickness, (b) negligible effect of length, and (c) joint angle showing minimal interaction effects confirming thickness as primary control parameter.

3.4.6. Peak crush force

When it comes to the influence of the variables strut thickness and length on PCF as shown in Fig. 17, it can be seen that the predominant factor influencing the peak crush forces of the auxetic structure is t_s . The linear increase in PCF is consistent with the increase in t_s , meaning that achieving low PCF requires using the lowest possible t_s . Although lower, the l_s can also be seen to influence PCF linearly following the same trend as that of t_s as shown in Fig. 17(b).

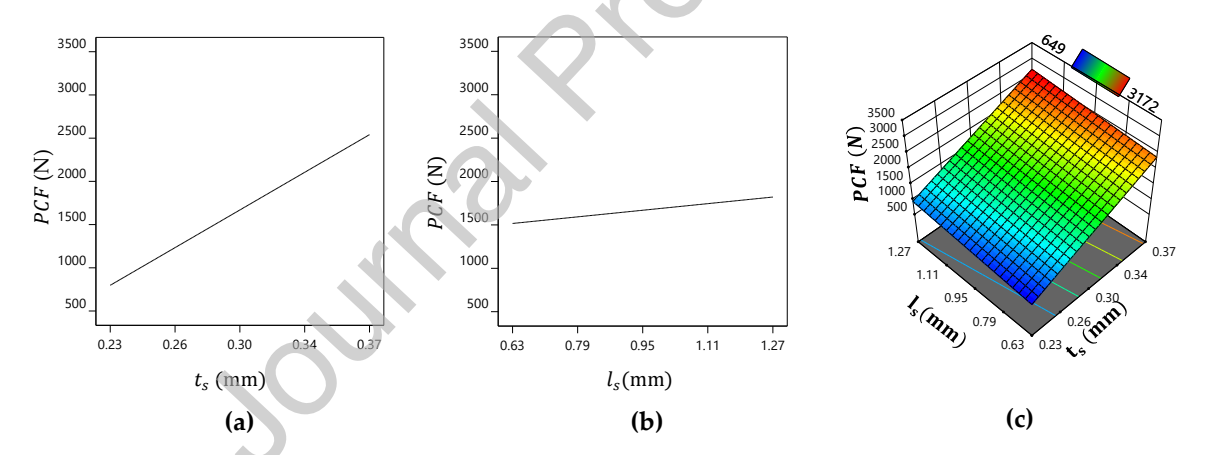


Fig. 17. Influence on peak crush force revealing (a) PCF increases linearly with strut thickness, (b) mild linear increase with length, and (c) combined effect showing peak PCF at highest t and L values.

However, the rate of increase in PCF with increasing l_s is significantly lower in comparison to t_s . Both effects are because of increased material which is increasing the threshed of stress required to initiate plastic failure as explained in the case of the yield strength. The interdependence of t_s and l_s on the PCF of the auxetic structure is shown in Fig. 17(c). Although PCF is susceptible to both t_s and l_s , the increase in PCF is predominantly driven by t_s in a linear fashion, with a very minimal influence from l_s . Nevertheless, the interaction effects indicate that the highest PCF is obtained when both t_s and l_s are at their highest values. Consequently, strut thickness has the most significant influence on PCF, followed by strut length, in the order of $t_s > l_s$.

3.5. Scenario tuning

3.5.1 Desirability mapping

The problem statement is formulated by integrating the objective function, design variables, and constraints. The primary objective is to meet the objective function by modifying the design variables t_s and l_s subject to the relevant constraints [131,132]. To achieve the best quantifiable performance within specific constraints [133], the optimisation problem necessitates the identification of appropriate design variables. Consequently, developing an optimal design necessitates defining a problem description that concentrates on the ideal responses. A single objective approach is insufficient when dealing with numerous responses, requiring the use of a multi-objective formulation to find the best solution. Consequently, to fulfil the scenario-based multi-objective criteria Eq. (11)-(14) are conceived for Scenario S1, S2 and S3 respectively with features as summarised in Table 3.

S1
$$\begin{cases} \text{Max. } E = f_1(t_s, l_s), \\ \text{Max. } \sigma_y = f_2(t_s, l_s), \\ \text{s. t. } 0.20 \le t_s \le 0.40, \\ \text{s. t. } 0.50 \le l_s \le 1.40, \end{cases}$$
 (11)

$$S2 \begin{cases} \text{Max. } SEA = f_3(t_s, l_s), \\ \text{Max. } CFE = f_4(t_s, l_s), \\ \text{Min. } PCF = f_5(t_s, l_s), \\ \text{s. t. } 0.20 \le t_s \le 0.40, \\ \text{s. t. } 0.50 \le l_s \le 1.40, \end{cases}$$

$$(12)$$

Max.
$$E = f_1(t_s, l_s)$$
,
Max. $\sigma_y = f_2(t_s, l_s)$,
Max. $SEA = f_3(t_s, l_s)$,
Max. $CFE = f_4(t_s, l_s)$,
Min. $PCF = f_5(t_s, l_s)$,
s.t. $0.20 \le t_s \le 0.40$,
s.t. $0.50 \le l_s \le 1.40$.

The optimisation solution is transformed into a desirability function utilising the desirability function approach. This technique employs a desirability function, denoted by D(X), as an objective function. It outlines the acceptable response ranges for each response (di), with desirability ranging from 0 to 1, identifying the least and most optimal solutions, respectively. When a response variable attains the target value, the desirability function value becomes 1, and when the response variable falls below the target value, the desirability function value decreases [395]. The geometric mean is employed to integrate the various desirability values, resulting in an overall desirability D, as indicated in Eq. (14):

$$D = (d_1 \cdot d_2 \cdot \dots \cdot d_n)^{\frac{1}{n}} = (\prod_{i=1}^n d_i)^{\frac{1}{n}}.$$
 (14)

3.5.2. Optimum design and validation

For simultaneous optimisation, each response was allotted a low and high value, as illustrated in Eq. (11)-(14) and solved utilising the desirability approach. The desirability scale is usually plotted from 0 to 1 where zero indicates the least optimum solution and 1 indicates the optimum ideal. The optimisation output as a function of the desirability objective for the three scenarios are presented in Figs.18 (a-c). For the target outcomes defined in scenarios S1, S2 and S3, the surrogate model offered solutions with a desirability of 0.79, 0.81 and 0.92 as summarised in Table 9. The resulting predictions in terms of the optimum strut thickness (t_s) length (l_s) that the auxetic architecture should feature to achieve the optimum solutions are also presented in Table 9.

Fig. 18(a) observed that the highest desirability score for S1 of 0.79 lies close to the lowest strut length (l_s), and higher strut thickness (t_s) which is 0.371 mm for t_s and 0.632 mm for l_s . For S2 as shown in Fig. 18(b), the highest desirability score of 0.81 lies close to the lowest strut thickness and strut length with the respective parametric being 0.304 mm and 1.268 mm respectively. Overall, S3 offered the highest desirability score of 0.92 at a higher strut length (1.268 mm) and lower strut thickness (0.229 mm).

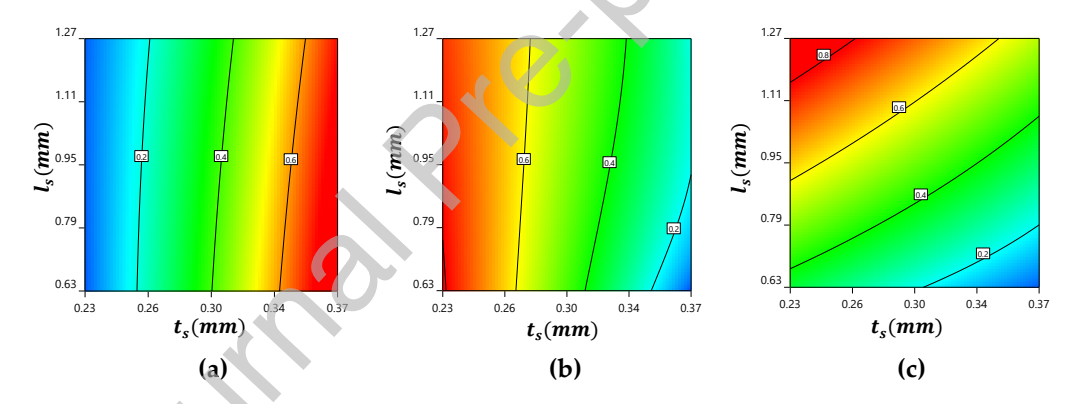


Fig. 18. Desirability plots for multi-objective optimisation scenarios revealing: (a) S1 prioritising stiffness and strength (desirability = 0.79); (b) S2 favouring crashworthiness (desirability = 0.81); (c) S3 achieving hybrid performance (desirability = 0.92)

Table 9. Optimal solution for SAS based for all the three scenarios considered.

Scenario	$t_s(mm)$	$l_s(mm)$	Porosity	Unit cell layers	Desirability
S1	0.371	0.632	67.2	5	0.79
S2	0.304	1.268	70.5	5	0.81
S3	0.229	1.268	73.4	5	0.92

Auxetic architecture satisfying the predicted optimum parameters Table 9 for all three scenarios were digitally conceived and numerically characterised using the finite element method, as shown in Fig. 19. with the resulting performance summarised in compared in Table 9. It can be seen from Fig.19(a) that comparatively stiffer and stronger auxetic architecture is revealed by the surrogate model to satisfy scenario 1 signified by the comparatively lower stress distribution under identical loading. The

architecture satisfying scenario 2 shown in Fig. 19(b) showed the highest stress profile making it suitable for energy absorption as opposed to mechanical performance. The architecture in Fig. 19(c) can be seen to exhibit a balanced performance between scenarios 1 and 3. Table 10 presents a comparison of the surrogate model and finite element prediction for the optimal architecture.

When it comes to scenario 1, the surrogate model predicts a negative Poisson's ratio with a value of -1.04, while FEA reports -1.07, resulting in a percentage difference of 2.8%. However, when it comes to *E*, the surrogate model was found to slightly overestimate the values compared to FEA. The surrogate model predicts 1023 MPa, resulting in a 3.23% difference from FEA value of 991 MPa. Similarly, the surrogate model slightly overestimated the yield strength, with a predicted value of 5.95 MPa compared to offering a difference of 4.75% in comparison to FEA. For scenario 2, the surrogate model and FEA are compared for their performance parameters for CFE resulting in a percentage difference of 3.51%. Furthermore, the surrogate model shows good agreement with FEA and SEA. The Surrogate Model predicts 14.48 kJ/kg, while FEA reports 14.14 kJ/kg, resulting in a percentage difference of 2.4%. This indicates a close approximation by the surrogate model for this parameter. The surrogate model also predicts a PCF of 1762 kN, while FEM reports 1850 kN, resulting 4.76% difference.

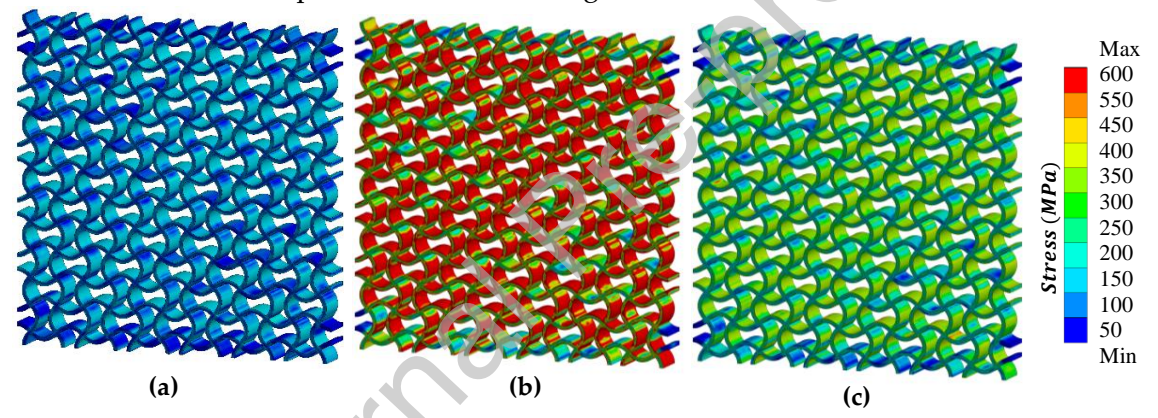


Fig. 19. Stress contour plots from FEA of optimised SAS designs for scenarios S1–S3: Scenario 1 yields the stiffest response, while S3 offers balanced stiffness and energy absorption under equivalent boundary conditions.

Table 10. Comparison between predicted and FEM values of optimum SAS architecture.

Item	Scenario 1			Scenario 2			Scenario 3		
	Pred.	FEA	%Δ	Pred.	FEA	%Δ	Pred.	FEA	%Δ
-v	-1.04	-1.07	2.80	-	-	-	-0.121	-0.125	3.20
E (MPa)	1023	991	3.23	-	-	-	761	771	1.29
σ_y (MPa)	5.95	5.68	4.75	-	-	-	5.53	5.69	2.96
CFE (%)	-	-	-	69.10	71.62	3.51	73.23	69.98	4.64
SEA (kJ/kg)	-	-	-	14.48	14.14	2.40	17.23	16.89	2.05
PCF (kN)	_	-	-	1762	1850	4.76	983	960	2.39

When it comes to scenario 3, the surrogate model provides predictions that closely align with FEA for -v. The surrogate model predicts -0.121, while FEM reports -0.125, resulting in a 3.2% difference.

Furthermore, the model prediction for E in this scenario demonstrates closer agreement with FEM. The surrogate model predicts 0761 GPa, resulting in a 1.29% difference in comparison to FEA, suggesting a relatively smaller deviation. Additionally, the surrogate model's prediction for σ_y is 5.53 MPa, resulting in a 2.96 2.96% all of which shows a close agreement between the two methods. The optimised SAS design (Scenario S3) achieved a maximum SEA of 17.23 kJ/kg and a CFE of 73.23%. To contextualise these results, values reported for other metallic auxetic structures fabricated via SLM, such as re-entrant and chiral geometries, typically fall within the ranges of 8–15 kJ/kg for SEA and 55% to 70% for CFE [134,135]. By contrast, conventional energy absorbers of comparable relative density, including honeycombs and metallic foams, generally achieve SEA values of 5–12 kJ/kg and CFE values of 50%–60% [136,137]. The comparison demonstrates that the optimised SAS structure not only outperforms conventional absorbers but also provides superior crashworthiness efficiency compared with established auxetic designs, underscoring both its novelty and competitiveness for energy-absorbing applications.

Overall, the predictions of the surrogate model are consistent with the desirability values with scenario 3 offering the closest agreement. Overall, the analysis of the three scenarios highlights that the surrogate model offers an accuracy of 95.24% which is consistent with the literature [116,129].

4. Conclusions

This study introduces a novel class of metallic auxetic metamaterials based on sinusoidal ligament architectures, fabricated using SLM processed AlSi10Mg. The auxetic behaviour, indicated by a negative Poisson's ratio of -0.113, was preserved despite geometric deviations and porosity (~9.3% reduction in relative density between CAD and printed prototypes) introduced during the SLM additive manufacturing process, demonstrating the robustness of the SAS design. Finite element simulations, validated to within 3.7% of experimental values, enabled predictive modelling of mechanical performance, and facilitated the development of statistically significant surrogate models ($R^2 > 0.92$) linking key geometrical parameters to performance responses. The surrogate models developed in this work are particularly significant in enabling rapid, computationally efficient design space exploration. By capturing nonlinear interactions between geometry and mechanical performance, these models eliminate the need for exhaustive experimental campaigns, offering predictive capability across a broad parametric range. The models identified strut thickness as the primary driver of elastic modulus (E up to 1023 MPa), yield strength (σ_v up to 7.8 MPa), and peak crush force (*PCF* up to 3171.8 N), while strut length exerted stronger control over auxeticity (v down to -0.123) and crush force efficiency (CFE up to 75.8%). Optimisation across three use-case scenarios namely, stiffness-driven, energy absorption-driven, and hybrid demonstrated design flexibility, with scenario S3 yielding the most balanced solution (SEA = 17.23 kJ/kg; CFE = 73.23%) at a desirability score of 0.92. These findings confirm that SAS architectures represent a promising pathway for high-performance, additively manufactured auxetic systems. The integration of predictive surrogate models with validated FEM offers a scalable methodology for future work on graded, hierarchical, or topology-optimised auxetic lattices in functional applications where impact mitigation and lightweight compliance are critical.

Declaration of competing interest

The authors declare that they have no known competing financial interests or personal relationships that could have influenced the work reported in this paper.

CRediT authorship contribution statement

Manpreet Singh: Writing – original draft, Methodology, Investigation, Formal analysis, Conceptualisation. Arun Arjunan: Writing – review & editing, Supervision, Resources, Project administration, Methodology, Investigation, Formal analysis. Ahmad Baroutaji: Writing – review & editing, Supervision, Resources, Project administration, Methodology, Investigation, Formal analysis. Chameekara T. Wanniarachchi: Writing – original draft, Methodology, Investigation, Formal analysis. John Robinson: Writing – original draft, Methodology, Investigation, Formal analysis. Abul Arafat: Writing – original draft, Methodology, Investigation, Formal analysis. Aaron Vance: Writing – original draft, Methodology, Investigation, Formal analysis. Oluwarotimi Lawal: Writing – original draft, Methodology, Investigation, Formal analysis. Martin Appiah: Writing – original draft, Methodology, Investigation, Formal analysis.

Acknowledgements

This work was supported by Innovate UK Smart Grant programme (Grant. No. 10033756).

References

- [1] X. Ma, D.Z. Zhang, M. Zhao, J. Jiang, F. Luo, H. Zhou, Mechanical and energy absorption properties of functionally graded lattice structures based on minimal curved surfaces, The International Journal of Advanced Manufacturing Technology 118 (2022) 995–1008. https://doi.org/10.1007/s00170-021-07768-y.
- [2] P. Zhang, Biligetu, D. Qi, R. Xue, K. Liu, Z. Huang, W. Wu, Y. Li, Mechanical design and energy absorption of 3D novel hybrid lattice metamaterials, Sci China Technol Sci 64 (2021) 2220–2228. https://doi.org/10.1007/s11431-020-1756-x.
- [3] B. Li, X. Xin, C. Lin, L. Liu, Y. Liu, J. Leng, Compressive properties and energy absorption of 4D printed auxetic mechanical metamaterials, Compos Struct 340 (2024). https://doi.org/10.1016/j.compstruct.2024.118135.
- [4] T. Yuxin, Z. Yifeng, Z. Yilin, L. Rong, Energy absorption characteristics and auxetic effect of novel elliptic-arc re-entrant honeycomb structures, Eng Struct 323 (2025) 119260. https://doi.org/https://doi.org/10.1016/j.engstruct.2024.119260.
- [5] C.W. Isaac, C.W. Isaac, F. Duddeck, structures for crashworthiness application a review Current trends in additively manufactured (3D printed) energy absorbing structures for crashworthiness

- application a review, Virtual Phys Prototyp 0 (2022) 1–44. https://doi.org/10.1080/17452759.2022.2074698.
- [6] J. Kang, M. Shirzad, J. Min Seok, W.-K. Jung, S.Y. Nam, Mechanical enhancement of porous scaffolds through integration of auxetic and conventional structures, Mater Lett 379 (2025) 137675. https://doi.org/https://doi.org/10.1016/j.matlet.2024.137675.
- [7] J. Zhong, C. Zhao, C. Chen, W.L. Lai, Q. Wang, Mechanical behaviors of composite auxetic structures under quasi-static compression and dynamic impact, European Journal of Mechanics A/Solids 109 (2025) 105454. https://doi.org/https://doi.org/10.1016/j.euromechsol.2024.105454.
- [8] G.-F. Li, H.-T. Liu, Tunable mechanical properties of the 3D anticircular-curve transversal-isotropic auxetic structure, Compos Struct 351 (2025) 118634. https://doi.org/https://doi.org/10.1016/j.compstruct.2024.118634.
- [9] X. Zhou, Y. Leng, A.K. Dutta, N. Juraev, A. Alkhayyat, Y. Elmasry, Machine learning analysis/optimization of auxetic performance of a polymeric meta-hybrid structure of re-entrant and meta-trichiral, European Journal of Mechanics A/Solids 109 (2025) 105463. https://doi.org/https://doi.org/10.1016/j.euromechsol.2024.105463.
- [10] K.E. Evans, Tensile network microstructures exhibiting negative Poisson's ratios, J Phys D Appl Phys 22 (1989) 1870–1876. https://doi.org/10.1088/0022-3727/22/12/011.
- [11] A. Pai, M. Rodriguez-Millan, M. Beppu, B. Valverde-Marcos, S.S. B., Experimental techniques for performance evaluation of shielding materials and configurations subjected to Blast and Ballistic impacts: A State-of-the-Art Review, Thin-Walled Structures 191 (2023) 111067. https://doi.org/https://doi.org/10.1016/j.tws.2023.111067.
- [12] M. Khajepour, A. Bayati, B. Rezaee, A. Khatami, M.A. Soltani, G. Faraji, K. Abrinia, M. Baghani, M. Baniassadi, Numerical and experimental investigation of 3D printed tunable stiffness metamaterial with real-time response using digital light processing technology, Journal of Materials Research and Technology 33 (2024) 480–490. https://doi.org/https://doi.org/10.1016/j.jmrt.2024.09.059.
- [13] M. Bera, 17 Auxetic textiles, in: S. Maity, K. Singha, P. Pandit (Eds.), Functional and Technical Textiles, Woodhead Publishing, 2023: pp. 543–614. https://doi.org/https://doi.org/10.1016/B978-0-323-91593-9.00001-8.
- [14] G. Chen, Y. Cheng, P. Zhang, S. Cai, J. Liu, Blast resistance of metallic double arrowhead honeycomb sandwich panels with different core configurations under the paper tube-guided air blast loading, Int J Mech Sci 201 (2021) 106457. https://doi.org/https://doi.org/10.1016/j.ijmecsci.2021.106457.
- [15] N. Mortazavi, S. Ziaei-Rad, Energy harvesting from vibrations of a beam under mass passage by arcshaped auxetic cantilever beams, European Journal of Mechanics A/Solids 109 (2025) 105432. https://doi.org/https://doi.org/10.1016/j.euromechsol.2024.105432.

- [16] T. Xue, W.Z. Jiang, Y. Zhang, N.C. Du, J.W. Shi, Y.C. Qu, X. Ren, A rotating triangular auxetic perforated plate: Structural design and characteristic analysis, Compos Struct 352 (2025) 118684. https://doi.org/https://doi.org/10.1016/j.compstruct.2024.118684.
- [17] H. Li, Y. Deng, Z. Zhang, J. Hou, J. Zhou, H. Wang, H. Zhang, X. Wang, Z. Guan, High-velocity impact characteristics of 3D auxetic composite cylindrical shell panels: Theory and experiment, Thin-Walled Structures 206 (2025) 112648. https://doi.org/https://doi.org/10.1016/j.tws.2024.112648.
- [18] E. Bahmanpour, A. Montazeri, A. Saeedi, M. Mahnama, Flexural behaviors of asymmetric Re-entrant auxetic honeycombs, European Journal of Mechanics A/Solids 109 (2025) 105475. https://doi.org/https://doi.org/10.1016/j.euromechsol.2024.105475.
- [19] Y.C. Qu, X.C. Teng, Y. Zhang, W.Z. Jiang, M.L. Xue, T. Xue, J.W. Shi, X. Ren, A novel 3D composite auxetic sandwich panel for energy absorption improvement, Eng Struct 322 (2025) 119129. https://doi.org/https://doi.org/10.1016/j.engstruct.2024.119129.
- [20] P. He, S. Wang, M. Zhang, L. Sang, L. Tong, W. Hou, Compression performance of 3D-printed thermoplastic auxetic structures, Thin-Walled Structures 197 (2024) 111558. https://doi.org/https://doi.org/10.1016/j.tws.2024.111558.
- [21] R.P. Bohara, S. Linforth, H.-T. Thai, T. Nguyen, A. Ghazlan, T. Ngo, Experimental, numerical, and theoretical crushing behaviour of an innovative auxetic structure fabricated through 3D printing, Thin-Walled Structures 182 (2023) 110209. https://doi.org/https://doi.org/10.1016/j.tws.2022.110209.
- [22] S. Bhardwaj, D.K. Mishra, Effect of different strut thickness on the mechanical behaviour of 3D printed auxetic structures, Mater Today Proc (2024). https://doi.org/https://doi.org/10.1016/j.matpr.2024.04.096.
- [23] O. Khaghani, D. Mostofinejad, S.M. Abtahi, Auxetic structures in civil engineering applications: Experimental (by 3D printing) and numerical investigation of mechanical behavior, Results in Materials 21 (2024) 100528. https://doi.org/https://doi.org/10.1016/j.rinma.2024.100528.
- [24] R.J.M. Bol, Y. Xu, B. Šavija, Printing path-dependent two-scale models for 3D printed planar auxetics by material extrusion, Addit Manuf 89 (2024) 104293. https://doi.org/https://doi.org/10.1016/j.addma.2024.104293.
- [25] N.K. Choudhry, B. Panda, S. Kumar, In-plane energy absorption characteristics of a modified re-entrant auxetic structure fabricated via 3D printing, Compos B Eng 228 (2022) 109437. https://doi.org/https://doi.org/10.1016/j.compositesb.2021.109437.
- [26] J. Wei, X. Hu, Y. Li, Z. Bian, K. Yan, D. Wu, 3D-Printed Piezoelectric Ceramics with Auxetic Structure for High-performance Sensing Applications, Ceram Int (2024). https://doi.org/https://doi.org/10.1016/j.ceramint.2024.11.234.
- [27] W. Yan, X. Tian, D. Zhang, Y. Zhou, Q. Wang, 3D Printing of Stretchable Strain Sensor Based on Continuous Fiber Reinforced Auxetic Structure, Chinese Journal of Mechanical Engineering: Additive Manufacturing Frontiers 2 (2023) 100073. https://doi.org/https://doi.org/10.1016/j.cjmeam.2023.100073.

- [28] Q. Shao, C. Ding, X. Ji, J. Mu, X. Wang, Y. Xue, Fabrication, microstructure and mechanical properties of a 3D re-entrant anti-trichiral honeycomb structure with excellent auxeticity and mechanical performance, Journal of Materials Research and Technology 32 (2024) 841–859. https://doi.org/https://doi.org/10.1016/j.jmrt.2024.07.098.
- [29] Y. Deng, Y. Jin, Compressive mechanical properties of a novel three-dimensional auxetic structure based on additive manufacturing, Thin-Walled Structures (2024) 112719. https://doi.org/https://doi.org/10.1016/j.tws.2024.112719.
- [30] J. Zhang, B. Song, Q. Wei, D. Bourell, Y. Shi, A review of selective laser melting of aluminum alloys: Processing, microstructure, property and developing trends, J Mater Sci Technol 35 (2019) 270–284. https://doi.org/10.1016/J.JMST.2018.09.004.
- [31] M. Lei, W. Hong, Z. Zhao, C. Hamel, M. Chen, H. Lu, H.J. Qi, 3D Printing of Auxetic Metamaterials with Digitally Reprogrammable Shape, ACS Appl Mater Interfaces 11 (2019) 22768–22776. https://doi.org/10.1021/acsami.9b06081.
- [32] P. Khanna, S. Sood, P. Mishra, V. Bharadwaj, A. Aggarwal, S.J. Singh, Analysis of compression and energy absorption behaviour of SLM printed AlSi10Mg triply periodic minimal surface lattice structures, Structures 64 (2024) 106580. https://doi.org/https://doi.org/10.1016/j.istruc.2024.106580.
- [33] Y. Jiang, B. Rudra, J. Shim, Y. Li, Limiting strain for auxeticity under large compressive Deformation: Chiral vs. re-entrant cellular solids, Int J Solids Struct 162 (2019) 87–95. https://doi.org/10.1016/J.IJSOLSTR.2018.11.035.
- [34] X.T. Wang, B. Wang, X.W. Li, L. Ma, Mechanical properties of 3D re-entrant auxetic cellular structures, Int J Mech Sci 131–132 (2017) 396–407. https://doi.org/10.1016/j.ijmecsci.2017.05.048.
- [35] W. Liu, N. Wang, T. Luo, Z. Lin, In-plane dynamic crushing of re-entrant auxetic cellular structure, Mater Des 100 (2016) 84–91. https://doi.org/10.1016/j.matdes.2016.03.086.
- [36] A. Spagnoli, R. Brighenti, M. Lanfranchi, F. Soncini, On the Auxetic Behaviour of Metamaterials with Re-entrant Cell Structures, Procedia Eng 109 (2015) 410–417. https://doi.org/10.1016/J.PROENG.2015.06.252.
- [37] A. Spagnoli, R. Brighenti, M. Lanfranchi, F. Soncini, On the Auxetic Behaviour of Metamaterials with Re-entrant Cell Structures, Procedia Eng 109 (2015) 410–417. https://doi.org/https://doi.org/10.1016/j.proeng.2015.06.252.
- [38] B. Nečemer, J. Kramberger, T. Vuherer, S. Glodež, Fatigue crack initiation and propagation in reentrant auxetic cellular structures, Int J Fatigue 126 (2019) 241–247. https://doi.org/10.1016/J.IJFATIGUE.2019.05.010.
- [39] A. Spagnoli, R. Brighenti, M. Lanfranchi, F. Soncini, On the Auxetic Behaviour of Metamaterials with Re-entrant Cell Structures, Procedia Eng 109 (2015) 410–417. https://doi.org/10.1016/j.proeng.2015.06.252.

- [40] X. Zhang, D. Yang, Mechanical properties of auxetic cellular material consisting of re-entrant hexagonal honeycombs, Materials 9 (2016). https://doi.org/10.3390/ma9110900.
- [41] Y. Jiang, Y. Li, 3D Printed Auxetic Mechanical Metamaterial with Chiral Cells and Re-entrant Cores, Scientific Reports 2018 8:1 8 (2018) 1–11. https://doi.org/10.1038/s41598-018-20795-2.
- [42] L. Yang, O. Harrysson, H. West, D. Cormier, Mechanical properties of 3D re-entrant honeycomb auxetic structures realized via additive manufacturing, Int J Solids Struct 69–70 (2015) 475–490. https://doi.org/10.1016/j.ijsolstr.2015.05.005.
- [43] E. Etemadi, M. Hosseinabadi, M. Taghizadeh, F. Scarpa, H. Hu, Enhancing the energy absorption capability of auxetic metamaterials through auxetic cells within re-entrant circular units, Eng Struct 315 (2024). https://doi.org/10.1016/j.engstruct.2024.118379.
- [44] H. Wang, Z. Lu, Z. Yang, X. Li, A novel re-entrant auxetic honeycomb with enhanced in-plane impact resistance, Compos Struct 208 (2019) 758–770. https://doi.org/10.1016/J.COMPSTRUCT.2018.10.024.
- [45] L. Yang, O. Harrysson, H. West, D.C.-I.J. of Solids, undefined 2015. Mechanical properties of 3D reentrant honeycomb auxetic structures realized via additive manufacturing, Elsevier (n.d.). https://www.sciencedirect.com/science/article/pii/S0020768315002152 (accessed February 23, 2023).
- [46] L. Yang, O. Harrysson, H. West, D.C.-I.J. of Solids, undefined 2015, Mechanical properties of 3D reentrant honeycomb auxetic structures realized via additive manufacturing, Elsevier (n.d.). https://www.sciencedirect.com/science/article/pii/S0020768315002152 (accessed February 23, 2023).
- [47] L. Yang, O. Harrysson, H. West, D.C.-I.J. of Solids, undefined 2015, Mechanical properties of 3D reentrant honeycomb auxetic structures realized via additive manufacturing, Elsevier (n.d.). https://www.sciencedirect.com/science/article/pii/S0020768315002152 (accessed February 23, 2023).
- [48] Y. Jiang, Y. Li, Novel 3D-Printed Hybrid Auxetic Mechanical Metamaterial with Chirality-Induced Sequential Cell Opening Mechanisms, Adv Eng Mater 20 (2018) 1700744. https://doi.org/https://doi.org/10.1002/adem.201700744.
- [49] D. Mousanezhad, B. Haghpanah, R. Ghosh, A.M. Hamouda, H. Nayeb-Hashemi, A. Vaziri, Elastic properties of chiral, anti-chiral, and hierarchical honeycombs: A simple energy-based approach, Theoretical and Applied Mechanics Letters 6 (2016) 81–96. https://doi.org/10.1016/j.taml.2016.02.004.
- [50] D. Mousanezhad, B. Haghpanah, R. Ghosh, A.M. Hamouda, H. Nayeb-Hashemi, A. Vaziri, Elastic properties of chiral, anti-chiral, and hierarchical honeycombs: A simple energy-based approach, Theoretical and Applied Mechanics Letters 6 (2016) 81–96. https://doi.org/10.1016/J.TAML.2016.02.004.
- [51] S. Jin, Y.P. Korkolis, Y. Li, Shear resistance of an auxetic chiral mechanical metamaterial, Int J Solids Struct 174–175 (2019) 28–37. https://doi.org/10.1016/J.IJSOLSTR.2019.06.005.
- [52] Q. Wang, Z. Yang, Z. Lu, X. Li, Mechanical responses of 3D cross-chiral auxetic materials under uniaxial compression, Mater Des 186 (2020) 108226. https://doi.org/10.1016/j.matdes.2019.108226.

- [53] X. Fei, L. Jin, X. Zhang, X. Li, M. Lu, Three-dimensional anti-chiral auxetic metamaterial with tunable phononic bandgap, Appl Phys Lett 116 (2020) 21902. https://doi.org/10.1063/1.5132589.
- [54] N. Novak, L. Krstulović-Opara, Z. Ren, M. Vesenjak, Mechanical properties of hybrid metamaterial with auxetic chiral cellular structure and silicon filler, Compos Struct 234 (2020) 111718. https://doi.org/10.1016/J.COMPSTRUCT.2019.111718.
- [55] Y. Jiang, Y. Li, 3D Printed Chiral Cellular Solids with Amplified Auxetic Effects Due to Elevated Internal Rotation, Adv Eng Mater 19 (2017). https://doi.org/10.1002/adem.201600609.
- [56] E. Etemadi, M. Hosseinabadi, M. Taghizadeh, F. Scarpa, H. Hu, Enhancing the energy absorption capability of auxetic metamaterials through auxetic cells within re-entrant circular units, Eng Struct 315 (2024) 118379. https://doi.org/https://doi.org/10.1016/j.engstruct.2024.118379.
- [57] E. Etemadi, A.M.M. Zamani, F. Scarpa, M. Zeeshan, M. Hosseinabadi, H. Hu, Modified re-entrant auxetic metamaterials with energy absorption enhancement, Mater Today Commun 38 (2024) 108079. https://doi.org/https://doi.org/10.1016/j.mtcomm.2024.108079.
- [58] X. Zhou, Y. Leng, A.K. Dutta, N. Juraev, A. Alkhayyat, Y. Elmasry, Machine learning analysis/optimization of auxetic performance of a polymeric meta-hybrid structure of re-entrant and meta-trichiral, European Journal of Mechanics A/Solids 109 (2025) 105463. https://doi.org/https://doi.org/10.1016/j.euromechsol.2024.105463.
- [59] Q. Zhang, X. Yu, Y. Xia, D. Zhang, R.S. Lakes, K.W. Wojciechowski, F. Scarpa, The shear performance of uniaxially thermoformed auxetic polymer foams, Compos B Eng 286 (2024) 111791. https://doi.org/https://doi.org/10.1016/j.compositesb.2024.111791.
- [60] N. Tripathi, D.S. Bag, M. Dwivedi, A Review on Auxetic Polymeric Materials: Synthetic Methodology, Characterization and their Applications, Journal of Polymer Materials 40 (2024) 227–269. https://doi.org/https://doi.org/10.32381/JPM.2023.40.3-4.8.
- [61] A. Amendola, F. Fraternali, Incremental auxetic response of composite lattices under isotropic prestress, Compos Struct 191 (2018) 145–153. https://doi.org/10.1016/j.compstruct.2018.02.020.
- [62] M.F. Ashby, The properties of foams and lattices, (n.d.). https://doi.org/10.1098/rsta.2005.1678.
- [63] X.-L. Peng, S. Bargmann, Tunable auxeticity and isotropic negative thermal expansion in three-dimensional lattice structures of cubic symmetry, Extreme Mech Lett 43 (2021) 101201. https://doi.org/https://doi.org/10.1016/j.eml.2021.101201.
- [64] M. Bambach, M.R. Tucker, Laser powder bed fusion of planar bi-metallic thermally auxetic lattice structures, CIRP Annals 73 (2024) 141–144. https://doi.org/https://doi.org/10.1016/j.cirp.2024.04.023.
- [65] C.S. Ha, M.E. Plesha, R.S. Lakes, Chiral three-dimensional lattices with tunable Poisson's ratio, Smart Mater Struct 25 (2016) 054005. https://doi.org/10.1088/0964-1726/25/5/054005.

- [66] L. Cabras, M. Brun, A class of auxetic three-dimensional lattices, J Mech Phys Solids 91 (2016) 56–72. https://doi.org/10.1016/J.JMPS.2016.02.010.
- [67] T. Fu, X. Hu, C. Yang, Impact response analysis of stiffened sandwich functionally graded porous materials doubly-curved shell with re-entrant honeycomb auxetic core, Appl Math Model 124 (2023) 553–575. https://doi.org/10.1016/J.APM.2023.08.024.
- [68] K. Xie, H. Chen, Y. Wang, J. Li, F. Jin, Nonlinear dynamic analysis of a geometrically imperfect sandwich beam with functionally graded material facets and auxetic honeycomb core in thermal environment, Aerosp Sci Technol 144 (2024) 108794. https://doi.org/10.1016/J.AST.2023.108794.
- [69] M. Simons, K. Digumarti, A. Conn, J. Rossiter, Tiled Auxetic Cylinders for Soft Robots, 2019. https://doi.org/10.1109/ROBOSOFT.2019.8722742.
- [70] D. Li, J. Yin, L. Dong, R.S. Lakes, Strong re-entrant cellular structures with negative Poisson's ratio, J Mater Sci 53 (2018) 3493–3499. https://doi.org/10.1007/s10853-017-1809-8.
- [71] R. LAKES, Foam Structures with a Negative Poisson's Ratio, Science (1979) 235 (1987) 1038–1040. https://doi.org/10.1126/science.235.4792.1038.
- [72] D. Prall, R.S. Lakes, Properties of a chiral honeycomb with a poisson's ratio of 1, Int J Mech Sci 39 (1997) 305–314. https://doi.org/10.1016/S0020-7403(96)00025-2.
- [73] M.F. Ashby, The properties of foams and lattices, Philosophical Transactions of the Royal Society A: Mathematical, Physical and Engineering Sciences 364 (2006) 15–30. https://doi.org/10.1098/rsta.2005.1678.
- [74] P. Koudelka, O. Jiroušek, T. Fíla, T. Doktor, Compressive properties of auxetic structures produced with direct 3D printing, Materiali in Tehnologije 50 (2016) 311–317. https://doi.org/10.17222/mit.2014.204.
- [75] S.Y. Choy, C.-N. Sun, K.F. Leong, J. Wei, Compressive properties of functionally graded lattice structures manufactured by selective laser melting, Mater Des 131 (2017) 112–120. https://doi.org/10.1016/J.MATDES.2017.06.006.
- [76] S.Y. Choy, C.N. Sun, K.F. Leong, J. Wei, Compressive properties of functionally graded lattice structures manufactured by selective laser melting, Mater Des 131 (2017) 112–120. https://doi.org/10.1016/j.matdes.2017.06.006.
- [77] D. Brackett, I. Ashcroft, R. Hague, Topology optimization for additive manufacturing, 22nd Annual International Solid Freeform Fabrication Symposium An Additive Manufacturing Conference, SFF 2011 (2011) 348–362.
- [78] C. Emmelmann, D. Herzog, J. Kranz, 10 Design for laser additive manufacturing, in: M. Brandt (Ed.), Laser Additive Manufacturing, Woodhead Publishing, 2017: pp. 259–279. https://doi.org/https://doi.org/10.1016/B978-0-08-100433-3.00010-5.

- [79] D. Thomas, The development of design rules for selective laser melting, in: 2009. https://api.semanticscholar.org/CorpusID:135739744.
- [80] I. Gibson, D. Rosen, B. Stucker, Additive Manufacturing Technologies, Springer New York, NY, 2015. https://doi.org/10.1007/978-1-4939-2113-3.
- [81] D. Li, L. Dong, R.S. Lakes, A unit cell structure with tunable Poisson's ratio from positive to negative, Mater Lett 164 (2016) 456–459. https://doi.org/10.1016/J.MATLET.2015.11.037.
- [82] M. Lei, W. Hong, Z. Zhao, C. Hamel, M. Chen, H. Lu, H.J. Qi, 3D Printing of Auxetic Metamaterials with Digitally Reprogrammable Shape, ACS Appl Mater Interfaces (2019). https://doi.org/10.1021/ACSAMI.9B06081/SUPPL_FILE/AM9B06081_SI_004.MP4.
- [83] K. Kempen, L. Thijs, J. Van Humbeeck, J.P. Kruth, Processing AlSi10Mg by selective laser melting: Parameter optimisation and material characterisation, Materials Science and Technology (United Kingdom) 31 (2015) 917–923. https://doi.org/10.1179/1743284714Y.0000000702.
- [84] Y. Hou, Y. Li, X. Cai, C. Pan, J. Wang, W. Zhang, P. Xu, Z. Fan, Y. Gao, Z. Li, J. Li, H. Sun, W. Huang, W. Yang, Mechanical response and response mechanism of AlSi10Mg porous structures manufactured by laser powder bed fusion: Experimental, theoretical and numerical studies, Materials Science and Engineering: A 849 (2022) 143381. https://doi.org/10.1016/J.MSEA.2022.143381.
- [85] EOS, EOS_Aluminium_AlSi10Mg_en, (n.d.). https://fathommfg.com/wp-content/uploads/2020/11/EOS_Aluminium_AlSi10Mg_en.pdf (accessed September 28, 2022).
- [86] N. Read, W. Wang, K. Essa, M.M. Attallah, Selective laser melting of AlSi10Mg alloy: Process optimisation and mechanical properties development, Materials & Design (1980-2015) 65 (2015) 417–424. https://doi.org/10.1016/j.matdes.2014.09.044.
- [87] X. Liu, C. Zhao, X. Zhou, Z. Shen, W. Liu, Microstructure of selective laser melted AlSi10Mg alloy, Mater Des 168 (2019) 107677. https://doi.org/10.1016/J.MATDES.2019.107677.
- [88] Mid-Size Metal 3D Printer for all kind of materials, (n.d.). https://www.eos.info/en/additive-manufacturing/3d-printing-metal/eos-metal-systems/eos-m-290 (accessed September 30, 2022).
- [89] M. Ulbin, M. Borovinšek, M. Vesenjak, S. Glodež, Computational Fatigue Analysis of Auxetic Cellular Structures Made of SLM AlSi10Mg Alloy, Metals (Basel) 10 (2020) 945. https://doi.org/10.3390/met10070945.
- [90] D. Syrlybayev, A. Perveen, D. Talamona, Controlling mechanical properties and energy absorption in AlSi10Mg lattice structures through solution and aging heat treatments, Materials Science and Engineering: A 889 (2024) 145843. https://doi.org/https://doi.org/10.1016/j.msea.2023.145843.
- [91] A. Baroutaji, A. Arjunan, G. Singh, J. Robinson, Crushing and energy absorption properties of additively manufactured concave thin-walled tubes, Results in Engineering 14 (2022) 100424. https://doi.org/10.1016/j.rineng.2022.100424.

- [92] M. Tang, P.C. Pistorius, Oxides, porosity and fatigue performance of AlSi10Mg parts produced by selective laser melting, Int J Fatigue 94 (2017) 192–201. https://doi.org/10.1016/J.IJFATIGUE.2016.06.002.
- [93] A. Baroutaji, A. Arjunan, M. Stanford, J. Robinson, A.G. Olabi, Deformation and energy absorption of additively manufactured functionally graded thickness thin-walled circular tubes under lateral crushing, Eng Struct 226 (2021) 111324. https://doi.org/10.1016/J.ENGSTRUCT.2020.111324.
- [94] C. Amini, R. Jerez-Mesa, J.A. Travieso-Rodriguez, J. Llumà, A. Estevez-Urra, Finite element analysis of ball burnishing on ball-end milled surfaces considering their original topology and residual stress, Metals (Basel) 10 (2020). https://doi.org/10.3390/MET10050638.
- [95] I. Mohamed, S. Şimşek, V. Kahya, D. Lanc, Computational modeling of functionally graded sandwich beams with porous core using an Ansys APDL-based approach, Mechanics Based Design of Structures and Machines (n.d.) 1–22. https://doi.org/10.1080/15397734.2024.2448715.
- [96] M.J.N. Priestley, ANALYSIS AND DESIGN OF CIRCULAR PRESTRESSED CONCRETE STORAGE TANKS., Journal - Prestressed Concrete Institute 30 (1985) 64–85. https://doi.org/10.15554/pcij.07011985.64.85.
- [97] E.M. Alawadhi, Meshing guide, Finite Element Simulations Using ANSYS (2020) 407–424. https://doi.org/10.1201/B18949-12/MESHING-GUIDE-ESAM-ALAWADHI.
- [98] M. Gómez-Castañeda, E. Cuan-Urquizo, A.L. Giraldo-Betancur, C. Félix-Martínez, A. Gómez-Ortega, J.M. Alvarado-Orozco, Additive manufacturing and mechanical characterization of sinusoidal-based lattice structures: a numerical and experimental approach, Progress in Additive Manufacturing 9 (2024) 315–330. https://doi.org/10.1007/s40964-023-00453-4.
- [99] T. Strek, H. Jopek, K.W. Wojciechowski, The influence of large deformations on mechanical properties of sinusoidal ligament structures, Smart Mater Struct 25 (2016) 54002. https://doi.org/10.1088/0964-1726/25/5/054002.
- [100] S. Okereke M. and Keates, Finite Element Mesh Generation, in: Finite Element Applications: A Practical Guide to the FEM Process, Springer International Publishing, Cham, 2018: pp. 165–186. https://doi.org/10.1007/978-3-319-67125-3_6.
- [101] W.D. Callister, Materials science and engineering: an introduction, 5th ed., Wiley, New York, 2000.
- [102] M. Omidi, A. Fatehinya, M. Farahani, Z. Akbari, S. Shahmoradi, F. Yazdian, M. Tahriri, K. Moharamzadeh, L. Tayebi, D. Vashaee, Characterization of biomaterials, Biomaterials for Oral and Dental Tissue Engineering (2017) 97–115. https://doi.org/10.1016/B978-0-08-100961-1.00007-4.
- [103] V. Mikli, H. Käerdi, P. Kulu, M. Besterci, CHARACTERIZATION OF POWDER PARTICLE MORPHOLOGY, Undefined 7 (2001) 22. https://doi.org/10.3176/ENG.2001.1.03.

- [104] P. Raghavendra, T. Pullaiah, Biomedical Imaging Role in Cellular and Molecular Diagnostics, Advances in Cell and Molecular Diagnostics (2018) 85–111. https://doi.org/10.1016/B978-0-12-813679-9.00004-X.
- [105] J.P. Kruth, L. Froyen, J. Van Vaerenbergh, P. Mercelis, M. Rombouts, B. Lauwers, Selective laser melting of iron-based powder, J Mater Process Technol 149 (2004) 616–622. https://doi.org/https://doi.org/10.1016/j.jmatprotec.2003.11.051.
- [106] H. Gong, K. Rafi, H. Gu, T. Starr, B. Stucker, Analysis of defect generation in Ti–6Al–4V parts made using powder bed fusion additive manufacturing processes, Addit Manuf 1–4 (2014) 87–98. https://doi.org/https://doi.org/10.1016/j.addma.2014.08.002.
- [107] E.R. Denlinger, M. Gouge, J. Irwin, P. Michaleris, Thermomechanical model development and in situ experimental validation of the Laser Powder-Bed Fusion process, Addit Manuf 16 (2017) 73–80. https://doi.org/https://doi.org/10.1016/j.addma.2017.05.001.
- [108] H. Lian, L. Zhang, Z. Meng, Biomimetic hydroxyapatite/gelatin composites for bone tissue regeneration: Fabrication, characterization, and osteogenic differentiation in vitro, Mater Des 156 (2018) 381–388. https://doi.org/https://doi.org/10.1016/j.matdes 2018.07.009.
- [109] A. Arjunan, S. Zahid, A. Baroutaji, J. Robinson, 3D printed auxetic nasopharyngeal swabs for COVID-19 sample collection, J Mech Behav Biomed Mater 114 (2021) 104175. https://doi.org/10.1016/j.jmbbm.2020.104175.
- [110] C.T. Wanniarachchi, A. Arjunan, A. Baroutaji, M. Singh, J. Robinson, A. Vance, M. Appiah, A. Arafat, 3D printed CoCrMo personalised load-bearing meta-scaffold for critical size tibial reconstruction, Annals of 3D Printed Medicine 15 (2024). https://doi.org/10.1016/j.stlm.2024.100163.
- [111] R. V Lenth, Response-surface methods in R, using RSM, J Stat Softw 32 (2009) 1–17. https://doi.org/10.18637/jss.v032.i07.
- [112] R.L. Lorza, M.Á.M. Calvo, C.B. Labari, P.J.R. Fuente, Using the multi-response method with desirability functions to optimize the Zinc electroplating of steel screws, Metals (Basel) 8 (2018) 1–20. https://doi.org/10.3390/met8090711.
- [113] A.I. Khuri, S. Mukhopadhyay, Response surface methodology, Wiley Interdiscip Rev Comput Stat 2 (2010) 128–149. https://doi.org/10.1002/wics.73.
- [114] N. Gunantara, A review of multi-objective optimization: Methods and its applications, Http://Www.Editorialmanager.Com/Cogenteng 5 (2018) 1–16. https://doi.org/10.1080/23311916.2018.1502242.
- [115] Multi-Objective Optimization, Multi-Objective Optimization (2018). https://doi.org/10.1007/978-981-13-1471-1.

- [116] A. Arjunan, S. Zahid, A. Baroutaji, J. Robinson, 3D printed auxetic nasopharyngeal swabs for COVID-19 sample collection, J Mech Behav Biomed Mater 114 (2020) 104175. https://doi.org/10.1016/j.jmbbm.2020.104175.
- [117] Engineering Design Optimization, (n.d.). https://mdobook.github.io/ (accessed May 10, 2023).
- [118] K. Bari, A. Arjunan, Extra low interstitial titanium based fully porous morphological bone scaffolds manufactured using selective laser melting, J Mech Behav Biomed Mater 95 (2019) 1–12. https://doi.org/10.1016/j.jmbbm.2019.03.025.
- [119] C. Pleass, S. Jothi, Influence of powder characteristics and additive manufacturing process parameters on the microstructure and mechanical behaviour of Inconel 625 fabricated by Selective Laser Melting, Addit Manuf 24 (2018) 419–431. https://doi.org/10.1016/j.addma.2018.09.023.
- [120] Y. Kang, J. Chang, Channels in a porous scaffold: A new player for vascularization, Regenerative Med 13 (2018) 705–715. https://doi.org/10.2217/rme-2018-0022.
- [121] A.A.A. Zadpoor, Mechanics of additively manufactured biomaterials, Elsevier Ltd, 2017. https://doi.org/10.1016/j.jmbbm.2017.03.018.
- [122] M. Benedetti, J. Klarin, F. Johansson, V. Fontanari, V. Luchin, G. Zappini, A. Molinari, Study of the compression behaviour of Ti6Al4V trabecular structures produced by additive laser manufacturing, Materials 12 (2019). https://doi.org/10.3390/ma12091471.
- [123] V. Weißmann, P. Drescher, R. Bader, H. Seitz, H. Hansmann, N. Laufer, Comparison of Single Ti 6 Al 4 V Struts Made Using Selective Laser Melting and Electron Beam Melting Subject to Part Orientation, Metals (Basel) (2017). https://doi.org/10.3390/met7030091.
- [124] M. De Wild, R. Schumacher, K. Mayer, E. Schkommodau, D. Thoma, M. Bredell, A. Kruse Gujer, K.W. Grätz, F.E. Weber, Bone regeneration by the osteoconductivity of porous titanium implants manufactured by selective laser melting: A histological and micro computed tomography study in the rabbit, Tissue Eng Part A 19 (2013) 2645–2654. https://doi.org/10.1089/ten.tea.2012.0753.
- [125] N. Taniguchi, S. Fujibayashi, M. Takemoto, K. Sasaki, B. Otsuki, T. Nakamura, T. Matsushita, T. Kokubo, S. Matsuda, Effect of pore size on bone ingrowth into porous titanium implants fabricated by additive manufacturing: An in vivo experiment, Materials Science and Engineering: C 59 (2016) 690–701. https://doi.org/10.1016/j.msec.2015.10.069.
- [126] A. Salimon, Y. Bréchet, M.F. Ashby, A.L. Greer, Potential applications for steel and titanium metal foams, J Mater Sci 40 (2005) 5793–5799. https://doi.org/10.1007/s10853-005-4993-x.
- [127] A. Arjunan, M. Singh, A. Baroutaji, C. Wang, Additively manufactured AlSi10Mg inherently stable thin and thick-walled lattice with negative Poisson's ratio, Compos Struct 247 (2020) 112469. https://doi.org/10.1016/j.compstruct.2020.112469.

- [128] A. Arjunan, M. Singh, A. Baroutaji, C. Wang, Additively manufactured AlSi10Mg inherently stable thin and thick-walled lattice with negative Poisson's ratio, Compos Struct 247 (2020) 112469. https://doi.org/10.1016/j.compstruct.2020.112469.
- [129] C.T. Wanniarachchi, A. Arjunan, A. Baroutaji, M. Singh, Mechanical performance of additively manufactured cobalt-chromium-molybdenum auxetic meta-biomaterial bone scaffolds, J Mech Behav Biomed Mater 134 (2022). https://doi.org/10.1016/j.jmbbm.2022.105409.
- [130] J. Fan, L. Zhang, S. Wei, Z. Zhang, S.-K. Choi, B. Song, Y. Shi, A review of additive manufacturing of metamaterials and developing trends, Materials Today 50 (2021) 303–328. https://doi.org/https://doi.org/10.1016/j.mattod.2021.04.019.
- [131] J.R.R.A. Martins, A. Ning, Engineering Design Optimization, Cambridge University Press, 2021. https://doi.org/10.1017/9781108980647.
- [132] A.A. Javadi, A. Faramarzi, R. Farmani, Design and optimization of microstructure of auxetic materials, Engineering Computations (Swansea, Wales) 29 (2012) 260–276. https://doi.org/10.1108/02644401211212398.
- [133] G.N. Vanderplaats, Design optimization A powerful tool for the competitive edge, 1st AIAA, Aircraft, Technology Integration, and Operations Forum (2001). https://doi.org/10.2514/6.2001-5214.
- [134] M. Lotfi, A. Masoumi, Experimental and numerical analysis of a novel 3D re-entrant auxetic structure, Proceedings of the Institution of Mechanical Engineers, Part D: Journal of Automobile Engineering 237 (2023) 3478–3493. https://doi.org/10.1177/09544070221139556.
- [135] T. Li, Y. Li, Mechanical behaviors of three-dimensional chiral mechanical metamaterials, Compos B Eng 270 (2024) 111141. https://doi.org/10.1016/J.COMPOSITESB.2023.111141.
- [136] C.W. Isaac, F. Duddeck, Recent progress in 4D printed energy-absorbing metamaterials and structures, Virtual Phys Prototyp 18 (2023). https://doi.org/10.1080/17452759.2023.2197436.
- [137] R. Nam, D. Nam, H.E. Naguib, Additive manufactured 3D re-entrant auxetic structures for enhanced impact resistance, Smart Mater Struct 33 (2024) 125021. https://doi.org/10.1088/1361-665X/ad8cb4.

Declaration of interests

⊠The authors declare that they have no known competing financial interests or personal relationships that could have appeared to influence the work reported in this paper.

☐The authors declare the following financial interests/personal relationships which may be considered as potential competing interests:

